Design and Optimization of Volumetric Solar Receivers based on Nanoparticles with Supercritical CO₂

D. C. Hernandez Aita



Design and Optimization of Volumetric Solar Receivers based on Nanoparticles with Supercritical CO₂

MASTER OF SCIENCE THESIS

For the degree of Master of Science in Mechanical Engineering at Delft University of Technology

D. C. Hernandez Aita

July 30, 2014





DELFT UNIVERSITY OF TECHNOLOGY DEPARTMENT OF PROCESS AND ENERGY

The undersigned hereby certify that they have read and recommend to the Faculty of Mechanical, Maritime and Materials Engineering (3mE) for acceptance a thesis entitled

Design and Optimization of Volumetric Solar Receivers based on Nanoparticles with Supercritical ${\rm CO_2}$

by

D. C. HERNANDEZ AITA

in partial fulfillment of the requirements for the degree of MASTER OF SCIENCE MECHANICAL ENGINEERING

| | Dated: <u>July 30, 2014</u> |
|----------------|-----------------------------|
| Supervisor(s): | Dr.ir.Rene Pečnik |
| | Ir.Ashish Patel |
| Reader(s): | Prof.dr.ir.Dirk Roekaerts |
| | Dr.ir.Rene Delfos |

Abstract

Solar thermal systems are becoming a popular alternative to reduce the environmental impact produced by power generation with fossil fuels due to its renewable and non-polluting nature. Most concentrated solar power (CSP) technologies today use selective surface-based collectors to convert the incident solar radiation into thermal energy. However, this kind of receiver has low energy conversion efficiency because of significant emissive losses at high temperatures. Volumetric solar receivers are an innovative technology that promise to increase the performance of CSP plants. In these collectors, concentrated solar radiation is directly absorbed by nanoparticles suspended in a base-fluid, which decreases the temperature difference between the absorber and the fluid, and reduces the emissive losses.

Several studies have been performed for volumetric absorption systems with conventional heat transfer fluids. In the present study, the feasibility of implementing carbon nanoparticles with supercritical carbon dioxide in a volumetric solar collector is investigated. The aim of this research is to combine a novel solar receiver technology with next-generation thermodynamic cycles, as s-CO₂ Brayton cycle, to reach unprecedented high efficiencies in CSP plants.

A two-dimensional combined radiative and heat transfer model is developed to predict the behavior of the nanofluid-based solar receiver. The model is used to propose design guidelines of the volumetric solar collector based on the optimum system efficiency. The advantages of implementing s-CO₂ are assessed by comparison with Therminol VP-1 at low inlet temperature. The performance of the system improves by 20%, and the outlet temperature of the receiver increases approximately 250°C when the base-fluid is substituted from Therminol VP-1 to s-CO₂. Moreover, the length of the solar collector reduces considerably, which decreases the cost and footprint of the equipment. Furthermore, the influence of varying the optical thickness τ , the receiver height H, and the solar concentration factor C is investigated. The result of the analysis shows that an ideal power generation cycle reaches efficiencies up to 60% when is coupled to a nanofluid-based solar collector, with s-CO₂ and carbon nanoparticles as working fluid, for $C \ge 10$, $H \ge 5cm$ and $\tau = 1.6$.

Volumetric solar receivers are compared to ideal surface solar receivers based on the optimum performance of the system. According to the results of this study, volumetric collectors with s-CO₂, as base fluid, have the potential to harness solar radiant energy more efficiently as

compared to conventional collectors for different configurations of receiver height and incident solar concentration.

Finally, the volumetric solar receiver, with s-CO₂ and carbon nanoparticles, is evaluated at a high inlet temperature of 675 K. The purpose of this investigation is to study if this new technology may be integrated into the s-CO₂ Brayton cycle for CSP plants. The result reveals that the performance of an ideal s-CO₂ Brayton cycle combined with the nanofluid-based solar collector has the potential to reach efficiencies up to 68% for C \geq 30 and H \geq 15cm.

Table of Contents

D. C. Hernandez Aita

| | Ack | nowledgements | ix |
|---|-------|---|----|
| 1 | Intro | oduction | 1 |
| | 1-1 | Concentrated Solar Power (CSP) Technologies | 2 |
| | 1-2 | Technology Outlook | 3 |
| | | 1-2-1 Supercritical CO ₂ Brayton Cycle | 3 |
| | | 1-2-2 Solar Receivers | 3 |
| | 1-3 | Motivation and Objective | 5 |
| 2 | Prop | perties of Nanofluids | 7 |
| | 2-1 | Thermal Transport Properties | 7 |
| | | 2-1-1 Density (ho) | 7 |
| | | 2-1-2 Specific Heat Capacity (Cp) | 7 |
| | | 2-1-3 Viscosity (μ) | 8 |
| | | 2-1-4 Thermal conductivity (k_c) | 8 |
| | 2-2 | Convective heat transfer coefficient (h_c) | 10 |
| | | 2-2-1 Solid-Liquid mixture | 10 |
| | | 2-2-2 Solid-Gas mixture | 11 |
| | 2-3 | Radiative Properties | 11 |
| | | 2-3-1 Radiative properties of s-CO $_2$ as base fluid | 11 |
| | | 2-3-2 Radiative properties of nanoparticles | 13 |
| | 2-4 | Optical Thickness | 16 |

Master of Science Thesis

v Table of Contents

| 3 | Nun | erical Modeling of the Volumetric Solar Receiver | 17 |
|---|-----|--|----|
| | 3-1 | Energy Balance | 17 |
| | | 3-1-1 Simplifications | 17 |
| | | 3-1-2 Energy Equation | 18 |
| | 3-2 | Thermal Radiation | 19 |
| | | 3-2-1 Simplifications | 19 |
| | | 3-2-2 Radiative Transfer Equation (RTE) | 20 |
| | | 3-2-3 RTE Solving Methodology | 21 |
| | | 3-2-4 Band I | 21 |
| | | 3-2-5 Band II | 24 |
| | 3-3 | Boundary Conditions | 25 |
| | 3-4 | Non-dimensional Form | 25 |
| | 3-5 | Numerical Method | 26 |
| 4 | Res | ts and Discussion | 27 |
| | 4-1 | System Performance | 27 |
| | | 4-1-1 Receiver Efficiency | 27 |
| | | 4-1-2 Overall System Efficiency | 28 |
| | 4-2 | Comparison of Therminol VP-1 and s- CO_2 as the base-fluid of a Volumetric Solar Receiver | 28 |
| | | 4-2-1 Parameter Analysis | 33 |
| | | 4-2-2 Comparison to surface-based solar receiver | 37 |
| | 4-3 | Volumetric Solar Receiver for the s-CO $_2$ Brayton Cycle $\dots \dots \dots \dots$ | 39 |
| 5 | Con | lusions and Recommendations | 43 |
| Α | MA | LAB Code | 45 |
| | A-1 | Volumetric solar receiver with variable properties | 45 |
| | | A-1-1 Volumetric Heat Generated | 50 |

List of Figures

| 1-1 | Conventional CSP technologies [3] | 2 |
|-----|---|----|
| 1-2 | Schematic of (a) surface absorption receiver and (b) volumetric absorption receiver [11] | 4 |
| 2-1 | Absorption characteristics of Carbon Dioxide at atmospheric conditions [39] | 12 |
| 2-2 | ${\rm CO_2}$ normalized absorption at different pressure and temperature. In the left the spectra at p=1 bar and T=349 K ($dash\ dot$); p=5 bar and T=429K ($black\ curve$); p=15 bar and T=544K ($dotted$); and p=23 bar and T=583K ($dashed$). In the right the spectra at p=9 bar and T=502K ($dash\ dot$); p=18 bar and T=563K ($black\ curve$); p=28 bar and T=600k ($dotted$); and p=32 bar and T=622K ($dashed$). Each spectrum is acquired with a resolution of 2 cm $^{-1}$ [40] | 12 |
| 2-3 | Effect of temperature (100.2-250 oF) and pressure (0-1500 psia) on the refractive index of carbon dioxide at $\lambda=0.6\mu m$ [45] | 13 |
| 2-4 | Boundary between the independent and the dependent scattering in the scattering regime [46] | 14 |
| 3-1 | 2-D steady-state model of a volumetric solar receiver. Figure adapted from reference [9] | 18 |
| 3-2 | Angle of refraction in the volumetric solar receiver | 19 |
| 3-3 | Distribution of concentrated solar irradiation and of a black body thermal emission | 21 |
| 3-4 | RTE distribution in Band I and Band II | 22 |
| 3-5 | Cumulating volumetric heat generated (—) for one-pass (a) and two-passes (b). Volumetric heat generated in each pass $()$ | 23 |
| 3-6 | Thermal Re-radiation as function of temperature | 24 |
| 4-1 | Properties of s-CO $_2$ as function of temperature at P $_0$ =250 bar | 30 |
| 4-2 | VP-1 (left column) and s-CO $_2$ (right column). (a) Transverse temperature profile at different axial locations. (b) Axial temperature profile at the top, middle and bottom of the receiver. Constant properties in <i>black</i> and variable properties in <i>red</i> . | 32 |

vi List of Figures

| 4-3 | Temperature contour within the volumetric receiver. (a) Therminol VP-1. (b) s- CO_2 with variable properties. | 32 |
|------|--|----|
| 4-4 | Receiver, carnot and system efficiencies as function of the dimensionless receiver lenght. (a) Therminol VP-1. (b) s-CO $_2$. Constant properties in <i>black</i> and variable properties in <i>red</i> | 33 |
| 4-5 | Optimum optical thickness τ^{opt} for the study case when C=10, H=2.5cm, T $_{in}$ =400K. (a) Therminol VP-1. (b) s-CO $_2$ | 34 |
| 4-6 | Variation of receiver height with constant C=10 and T $_{in}$ =400K. (a) Therminol VP-1 with $\tau_{VP-1}=1.2$. (b) s-CO $_2$ with $\tau_{s-CO_2}=1.6$. (c) Asymptotic-type curve for both fluids. Constant properties in <i>black</i> and variable properties in <i>red</i> . | 35 |
| 4-7 | Variation of solar concentration factor with constant H=2.5cm and T_{in} =400K. (a) Therminol VP-1 with $\tau_{VP-1}=1.2$. (b) s-CO $_2$ with $\tau_{s-CO_2}=1.6$. (c) Asymptotic-type curve for both fluids. Constant properties in <i>black</i> and variable properties in <i>red</i> | 36 |
| 4-8 | Spectral emissivity of an ideal selective surface-based receiver. (—) incident solar flux. () emissive losses | 37 |
| 4-9 | Surface Receiver vs. Volumetric Receiver for different solar concentration factors with constant $H=2.5 \text{cm}$, $T_{in}=400 \text{K}$. (a) Therminol VP-1 (b) s-CO ₂ . Constant properties in <i>black</i> and variable properties in <i>red</i> | 38 |
| 4-10 | Surface Receiver vs. Volumetric Receiver for different receiver height with constant C=10, T_{in} =400K. (a) Therminol VP-1. (b) s-CO ₂ . Constant properties in <i>black</i> and variable properties in <i>red</i> | 38 |
| 4-11 | s-CO $_2$ optimum system efficiency; effect of inlet temperature and properties variation. (a) Different solar concentration factor with constant H=2.5cm and τ =1.6. (b) Different receiver height with constant C=10 and τ =1.6. Constant properties in <i>black</i> and variable properties in <i>red</i> | 41 |

D. C. Hernandez Aita Master of Science Thesis

List of Tables

| 1-1 | Operating points of solar receivers [8] | | | | 3 |
|-----|---|--|--|--|---|
| 2-1 | Thermal Conductivity of several materials common in nanofluids [20] | | | | 9 |

Master of Science Thesis D. C. Hernandez Aita

viii List of Tables

Acknowledgements

I would like to thank my supervisor Dr.ir.Rene Pečnik for his support, guidance and enthusiasm. He gave me the motivation to challenge myself during these few months. I am also very thankful to my daily supervisor Ir.Ashish Patel for his willingness to help me during any hour of the day and for being so kind every time I had a question or doubt.

I would also like to express my gratitude to the examination committee for the time and effort devoted in reading and evaluating my thesis report.

I am very thankful to all my friends for making such a great time my two years in Delft. Special thanks to Gustavo for helping me and motivating me during this thesis.

Finally, I express my deepest gratitude to my loving family for constantly support me in all my decisions.

Delft, University of Technology July 30, 2014 D. C. Hernandez Aita

x Acknowledgements

D. C. Hernandez Aita



Chapter 1

Introduction

Ever since the Industrial Revolution took off in the 18th century, fossil fuels have become the first source of thermal energy conversion in the world. Currently, 80% of global energy consumption is based on fossil fuels [1]. Although coal, oil and natural gas have been suitable companions to human development, their disadvantages have become more evident with the increasing energy consumption. Global warming, air pollution, acid rain, and impact on aquatic life by oil spill, which are side effects produced by fossil fuels, are the driving forces that promote the research and implementation of cleaner energy conversion technologies. Moreover, fossil fuels are non-renewable, which means there is a limited amount of these resources available for the near future. For these reasons, the world needs to use energy consciously and generate it from more renewable sources.

Solar thermal systems are becoming a popular alternative to reduce the environmental impacts. These systems require no fossil fuel, and produce little environmental pollution during the manufacture, operation and decommissioning. Another important advantage of this technology compared to other technologies is its availability. The total solar energy flux intercepted by the earth on any particular day is $6.26 \cdot 10^{20}$ Joules per hour. This is equivalent to burning 360 billion tons of oil (toe) per day or 15 Billion toe per hour [2]. However, in 2013, the *BP Statistical Review of World Energy* reported a worldwide energy consumption of 12.5 Billion toe per year. This means that the earth receives more energy from the Sun in just one hour than the world's population uses in a whole year.

Solar energy can be converted into electricity in two different ways:

- *Photovoltaic systems*, which directly converts solar energy into electricity using a PV cell made of a semiconductor material.
- Solar power concentrators, which concentrate energy from the sun to heat a receiver to high temperatures. This heat is transformed first into mechanical energy by turbines, and then into electricity by a generator.

2 Introduction

1-1 Concentrated Solar Power (CSP) Technologies

Concentrated solar power technologies include solar trough, linear Fresnel, parabolic dish Stirling and power towers as illustrated in Figure 1-1. The CSP systems are typically integrated by a solar receiver, which collects the solar energy and converts it to heat, a power cycle, which converts the heat energy to electricity, and a thermal energy storage. Currently, there are hundreds of MW under construction, and thousands of MW under development worldwide. Spain and the United States together represent 90% of the market. Algeria, Egypt and Morocco are building integrated solar combined cycle plants, while Australia, China, India, Italy and the United Arab Emirates are finalising or considering projects [1].

Current CSP plants utilize oil, molten salts or direct steam, among others, to transfer solar energy to the power block. For example, most of the trough systems use large parabolic reflectors that have oil-filled pipes running along their center, or focal point. The mirrored reflectors are tilted toward the sun, and focus sunlight onto the pipes to heat the oil inside. The hot oil is then used to boil water, which makes steam to run conventional steam turbines. On the other hand, the use of steam as only heat transfer fluid has become popular. For instance, PS-10 is a solar concentration tower plant located in Seville, Spain that works with direct saturated steam to transfer the solar energy to the steam turbine [4]. Nonetheless, these fluids have properties that limit plant performance. For instance, the synthetic oil has an upper temperature limit of 400°C while direct steam generation requires complex controls and has limited storage capacity. Higher operating temperatures generally translate into higher thermal cycle efficiency and often allow for more efficient thermal storage. To obviate these limitations, alternative fluids are under investigation by research teams worldwide [5].



Figure 1-1: Conventional CSP technologies [3]

1-2 Technology Outlook

1-2-1 Supercritical CO₂ Brayton Cycle

The Supercritical carbon dioxide (s-CO₂) Brayton cycle is such an alternative and has emerged as a promising avenue for high-efficiency power production at temperatures relevant for CSP applications, due to small compression work and large regeneration power. It has high power density that is consequence of the high density of the working fluid under supercritical pressures. The compression, expansion, and heat rejection of the working fluid is under single phase, which reduces the complexity of the system [6]. Finally, the s-CO₂ Brayton cycle does not required a secondary cycle. The s-CO₂ transfers directly the solar energy to the turbine.

Moreover, CO₂ has significant advantages over other fluids for these kind of cycles [7]:

- The supercritical point of CO₂ is approximate 31 °C (the supercritical point for water is much higher (374 °C)), which is favorable for cooling of Brayton cycles entirely above the critical point.
- It is relatively inexpensive;
- It is stable and inert at the temperatures of interest;
- It is abundant and non-toxic.

It may be said that the supercritical CO₂ Brayton cycle with solar to thermal energy conversion systems are promising alternatives, which could reduce the environmental impacts and also increase greatly the cycle efficiency.

1-2-2 Solar Receivers

The objective of the solar receiver is to absorb as much sunlight as possible while limiting the radiative heat losses to the surroundings. To achieve high temperatures at the exit of the receiver, the incident solar radiation is concentrated using a field of reflective mirrors which focus the light into a line (in the case of parabolic trough) or into a point (in the case of power tower). These optical concentrating devices are described by their optical concentration factor (C), which is the ratio of the area of the input beam (mirrors) to the area of the output beam (solar concentrator). In order to illustrate the operating conditions of the solar receivers in the market, Table 1-1 shows a range of values for operating temperatures and optical concentration factors.

 System
 C
 Operating Temperature [°C]

 Flat Panel
 0.5-2
 100-300

 Adjustable Panel
 2-10
 100-300

 Trough & Fresnel
 15-100
 100-400

 Tower
 500-1000+
 500-1200+

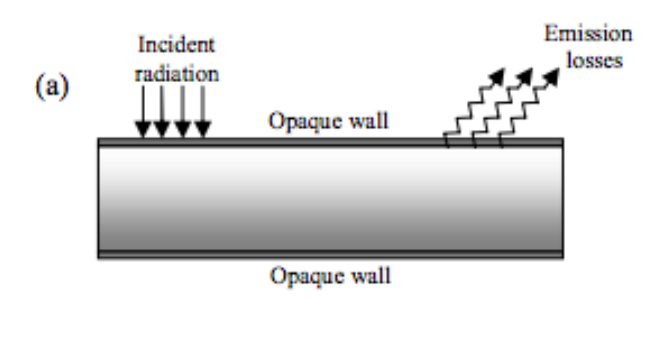
Table 1-1: Operating points of solar receivers [8]

4 Introduction

In a conventional solar thermal collector that contains a solid absorber, such as a flat absorber in a flat-plate collector, or parabolic reflectors in trough systems, sunlight is absorbed onto a solid surface (Figure 1-2 (a)). The surfaces are typically black or spectrally selective such that high absorptivity in the solar spectrum is coupled with low emissivity in the infrared (IR) spectrum [9]. Although surface-based receivers are efficient at solar-to-thermal conversion, they are not well suited for transferring heat to a carrier fluid. In particular, a large temperature difference between the absorber and the fluid arises at high levels of solar concentration. The temperature difference leads to significant emissive losses at the surface, which results in a low overall conversion efficiency of solar energy [10]. In order to overcome the drawbacks of these solid-surface receivers attempts have been made to use volumetric receivers.

Volumetric receivers promise to be more efficient than surface-based receivers for solar-to-thermal energy conversion for medium and high operating temperatures. In volumetric receivers, concentrated solar radiation is directly absorbed by nanoparticles suspended in the base-fluid, which decreases the temperature difference between the absorber and the fluid, and reduces the emissive losses at higher temperatures. The incident radiation being directly absorbed by the working fluid is illustrated by Figure 1-2 (b). The top wall is semi-transparent to solar radiation. Therefore, the entire volume of the working fluid participates in the conversion of solar energy to thermal energy via absorption of radiation.

Volumetric solar receiver using small particles has been investigated since the late 70s. Hunt [12] describes how a dispersion of small absorbing particles forms an ideal system to collect radiant energy, transform it to heat, and efficiently transfer the heat to a surrounding fluid. Moreover, he explained how this technology can be used to heat a compressed gas in an engine utilizing a Brayton cycle. Abdelrahman et.al [13] studied suspensions of solid particles in gases used for direct absorption of concentrated solar radiation. In his research,



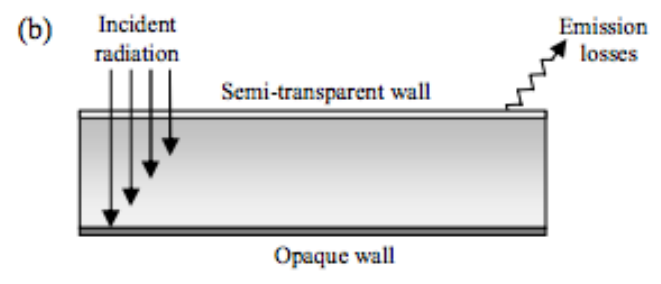


Figure 1-2: Schematic of (a) surface absorption receiver and (b) volumetric absorption receiver [11].

the absorption was found to be dependent on the imaginary part of the complex index of refraction of the material used and on the size of the particle. Recently, several theoretical and experimental studies have been performed for volumetric solar receiver with small particles in conventional fluids. A detailed mathematical model of the interaction of radiative flux with a convective transport in an absorbing, emitting and scattering falling film has been proposed by Kumar and Tien [14]. The model is evaluated for a volumetric receiver with nitrate salt, as base fluid, and cobalt oxide particles. The results showed than greater increases of film temperature were obtained when all the incident flux was absorbed by the particles. This was achieved by increasing the particle diameter, the particle volume fraction, or the film width. The thermo-physical properties of the film were also analysed. Kumar and Tien concluded that keeping constant the thermo-physical properties of the film and considering a gray medium (constant radiative properties), higher temperatures were predicted in the film. Lenert and Wang [10] presented a combined modeling and experimental study to optimize the efficiency of a volumetric solar receivers with Therminol VP-1, as base fluid, and carbon-coated nanoparticles. A one-dimensional transient heat transfer model was developed to investigate the effect of solar concentration, receiver height and optical thickness on receiver performance. The results showed that the efficiency of nanofluid volumetric receiver improves with increasing solar concentration and nanofluid height. Phelan et al. [9] theoretically investigates the feasibility of using a volumetric solar receiver, with water and aluminium particles as nanofluid, and compares its performance with a typical flat-plate receiver. A steady-state two-dimensional heat transfer model was developed with a radiative flux considering the effects of absorption and scattering within the nanofluid. He concluded that the presence of nanoparticles increases the absorption of incident radiation by more than 9 times over pure water. The results showed that the performance of the receiver varies between 30% and 80% for different values of inlet temperature of the nanofluid. The comparison with the flat-surface receiver, under similar operating conditions, illustrated that the efficiency of the volumetric receiver using nanofluid is 10% higher than that of a flat-plate receiver.

1-3 Motivation and Objective

Most of the studies for volumetric solar receiver have been performed with conventional base fluids in solar applications as Therminol VP-1 [10]. Moreover, some researchers have considered other type of fluids, such as glycols, molten salts, nitrate salts and organic fluids, as potential options [15]. However, most of these fluids work for low ($< 250^{\circ}C$) or medium ($250\text{-}500^{\circ}C$) temperatures. Therefore, finding reliable base fluids for direct absorption that can work at high-temperatures is a big challenge.

Supercritical CO_2 , as a base fluid, has not been considered in the past in volumetric solar receivers with nanoparticles. However, it has several advantages that make it a great option for solar applications. Carbon dioxide is readily available, inexpensive, non-toxic, chemically inert and environmentally acceptable [16]. Moreover, it is considered a good solvent for a variety of low molecular weight and non polar compounds [17]. Furthermore, s- CO_2 stands out from other fluids to be used in nanofluid-based solar receivers because is suitable to work in high temperature ranges (> $500^{\circ}C$). Almost any other conventional fluid used in solar applications can work at high temperatures.

The objective of this thesis is to study the feasibility of implementing supercritical carbon

6 Introduction

dioxide, as the base fluid, in a nanofluid-based volumetric solar receiver. The ambition of the investigation is to combine a new solar receiver technology with next-generation thermodynamic cycles, as s-CO $_2$ Brayton cycle, to reach unprecedented high efficiencies in CSP plants. The high CSP system performance will make this kind of technology more competitive (in terms of efficiency) in the area of power generation. Furthermore, it also seeks to make the s-CO $_2$ Brayton cycle a potential power conversion cycle to mitigate greenhouse gas emissions.

In order to achieve the aim of the thesis, several topics have been developed along this work.

- A literature survey of nanofluids. The thermo-physical and radiative properties of the nanofluids are discussed in chapter 2. Furthermore, the optical properties of s-CO₂ are investigated;
- 2. A numerical model for volumetric receivers with nanoparticles has been developed. The 2-D steady-state model has been documented in chapter 3;
- 3. A comparative analysis of Therminol VP-1 and s-CO₂ as the base fluids of the volumetric solar receiver has been presented in chapter 4;
- 4. A parameter study has been performed in chapter 4 to understand the influence of the optical thickness, the receiver height, and the solar concentration factor on the efficiency of the cycle;
- 5. A comparative analysis of a surface-based receiver and a nanofluid-based volumetric receiver based on the system performance has been discussed in chapter 4;
- 6. Finally, the performance of an ideal s-CO $_2$ Brayton cycle coupled with a volumetric solar receiver with inlet temperature of 675 K is presented in chapter 4.

D. C. Hernandez Aita Master of Science Thesis

Properties of Nanofluids

A nanofluid is defined as a modern engineering material that consists of solid particles suspended in a base-fluid with sizes typically ranging from 1 to 100 nm. Many researchers have indicated that compared to conventional heat transfer fluids, nanofluids feature enhanced thermo-physical properties such as viscosity and thermal conductivity, convective heat transfer coefficients, and optical properties [18]. In this chapter, a summary of different studies to estimate the thermo-physical properties of the nanofluids and the heat transfer coefficient is shown. These studies indicate that the addition of very small volume concentration $(\phi \leq 0.15)$ of nanoparticles enhance significantly the properties of the mixture. Furthermore, the radiative properties of the s-CO₂ and nanoparticles are described.

2-1 Thermal Transport Properties

2-1-1 Density (ρ)

The mass of the nanofluids (m), within the volume (V) is equal to the sum of the fluid and the solid masses as shown in equation (2-1) [19]. Therefore, the density of the mixture is the ratio of the mass of the nanofluids to its volume. The expression for density shown in equation (2-2) illustrates that for very low ϕ , the change in density is negligible.

$$m = [(1 - \phi)\rho_f + \phi\rho_p]V \tag{2-1}$$

$$\rho_{eff} = (1 - \phi)\rho_f + \phi\rho_p \tag{2-2}$$

Specific Heat Capacity (Cp)2-1-2

The specific heat capacity of nanofluids is defined as the mass-weighted average of the specific heat capacities of the constituent materials as given by equation (2-3) [20].

$$Cp_{eff} = \frac{1}{\rho_{eff}} [(1 - \phi)\rho_f Cp_f + \phi\rho_p Cp_p]$$
 (2-3)

2-1-3 Viscosity (μ)

The analytical investigations on the viscosity of fluids with small particles commenced with the study of Einstein [21]. He determined a formula for evaluating the effective viscosity (μ_{eff}) of a fluid of viscosity (μ_f) containing a dilute suspension of small rigid spherical particles. The formula is illustrated by equation (2-4).

$$\mu_{eff} = \mu_f (1 + 2.5\phi) \tag{2-4}$$

This relation is restricted for low volume concentration ($\phi < 0.05$). Einstein's equation was extended by Brinkman [22] to slightly denser concentrations of spheres:

$$\mu_{eff} = \mu_f \frac{1}{(1 - \phi)^{2.5}} \tag{2-5}$$

The brownian motion and its effects on viscosity were neglected in these studies. The brownian motion is the random motion of particles suspended in a fluid resulting from their collision with the quick atoms or molecules within the fluid. It is very important for nanoparticles. Therefore, Batchelor [23] performed an analytical study that took into account the effects of the Brownian motion of particles. The expression presented in equation (2-6) is applicable to very fine particles at concentrations up to $\phi = 0.1$:

$$\mu_{eff} = \mu_f (1 + 2.5\phi + 6.5\phi^2) \tag{2-6}$$

The correlations presented above are widely used by researchers to estimate the viscosity of nanofluids when experiments are not performed. However, one may find other correlations of the effective viscosity of the mixture in the literature [19]. Each relation has its own application limitation. There has not been a general study or an empirical correlation that applies to all types or even several types of base-fluid and nanoparticles [20]. The direct and reliable form to obtain the effective viscosity of the nanofluid is by experiment. Almost all the results of experimental studies of viscosity of nanofluids have shown significant differences to those of the analytical study. Several researchers have performed experimental studies to achieve accurate correlations for specific nanofluids. For example, Maïga et.al [24] has experimentally obtained expressions for the effective viscosity for ethylene glycol - γAl_2O_3 and water - γAl_2O_3 . Xuan and Li [25] have also experimentally measured the effective viscosity, but in this case for water - Cu nanofluid.

2-1-4 Thermal conductivity (k_c)

The effective thermal conductivity is considered one of the most important parameters to indicate the potential heat transfer enhancement of the nanofluid. Researchers have shown that the thermal conductivity of the nanofluid is a function of the thermal conductivity of the

base-fluid, the thermal conductivity of the nanoparticle, the volume fraction, the surface area, and the shape of the nanoparticles suspended in the fluid [26]. It is observed in Table 2-1 that the thermal conductivity of the solid particles are several orders of magnitude higher than the thermal conductivity of the base-fluid. Therefore, it is expected that adding particles in the base-fluid would result in an increase in the thermal conductivity of the mixture. Researchers developed several correlations to estimate how much the increase would be and many experiments have been conducted to compare experimental data with those of analytical models. The two most widely used correlations to calculate effective thermal conductivity of two-phase mixture were formulated by Maxwell and Hamilton-Crosser.

| Solids | $k_{c(p)} [W/mK]$ | Liquids | $k_{c(f)}$ [W/mK] |
|------------------|-------------------|-----------------|-------------------|
| Silver | ${427}$ | Water | 0.613 |
| Copper | 395 | Ethylene glycol | 0.253 |
| Aluminium | 237 | Engine oil | 0.145 |
| Carbon Nanotubes | 3200-3500 | Alcohol | 0.115 |
| Brass | 120 | Glycerol | 0.285 |
| Nickel | 91 | | |
| Alumina | 39 | | |

Table 2-1: Thermal Conductivity of several materials common in nanofluids [20]

The effective conductivity of a mixture, $k_{c(eff)}$, of solid spheres may be estimated by Maxwell's expression shown in equation (2-7) [20]. This correlation is only valid for a fluid that has lower thermal conductivity than the solid particles.

$$k_{c(eff)} = k_{c(f)} \left[1 + \frac{3(k_{c(p)} - k_{c(f)})\phi}{(k_{c(p)} - k_{c(f)}) - (k_{c(p)} - k_{c(f)})\phi} \right]$$
(2-7)

Hamilton and Crosser [27] extended Maxwell work to cover non spherical particles and introduced the shape factor n, which can be determined experimentally for different types of materials. Equation (2-8) shows the Hamilton and Crosser correlation.

$$k_{c(eff)} = k_{c(f)} \left[\frac{k_{c(p)} + k_{c(f)}(n-1) + (n-1)(k_{c(p)} - k_{c(f)})\phi}{k_{c(p)} + k_{c(f)}(n-1) - (k_{c(p)} - k_{c(f)})\phi} \right]$$
(2-8)

A comprehensive review of other analytical expressions and experimental works are given by [20, 28]. Most of the experiments are investigated with volume fractions in the range of 1-15% showing very promising results between 10-50% enhancements of thermal conductivity. Most of these experiments have been made with base-fluids and nanoparticle materials mentioned in Table 2-1. The Hamilton-Crosser model was found to be in agreement with experimental data for $\phi < 10\%$. However, the Maxwell model always predicted a lower thermal conductivity compared to experimental data [28].

2-2 Convective heat transfer coefficient (h_c)

The convective heat transfer coefficient is the parameter that best describes the performance of the fluid as a heat transfer medium. There are several studies to predict the h_c of nanofluids with both solid-liquid and solid-gas mixtures. All of these studies concluded that the heat transfer coefficient for a nanofluid is significantly higher than that of the base-fluid under the same flow conditions.

2-2-1 Solid-Liquid mixture

Most of the experimental studies that have measured directly the convective heat transfer of nanofluids are in laminar flow. Heris et.al [29] performed experimental investigations with water-Al₂O₃ nanofluid. In this work, laminar flow forced convection heat transfer of the nanofluid inside a circular pipe was investigated for different volume concentrations from 0.2% to 2.5%. The experiment showed an enhancement of heat transfer coefficient up to 40%due to the nanoparticles presence in the fluid. Heris et.al concluded that the heat transfer coefficient increases by increasing the concentration of nanoparticles in the nanofluid. Jung and Oh [30] also performed experimental investigations of h_c in laminar flow regime with water-Al₂O₃ nanofluid. Several values of ϕ were used to investigate the effect of volume concentration of nanoparticles to the convective heat transfer in microchannels. The h_c was measured to increase up to 32% compared with pure water, which follows the same trend as Heris et.al. Other nanoparticle materials have been used to investigate the convective heat transfer of nanofluids. Xuan and Li [31] built an experimental system to measure the convective heat transfer coefficient of Cu-water nanofluid. The experimental results showed that the suspended nanoparticles increase the convective heat transfer coefficient up to 60% for the nanofluid, with $\phi=2.0\%$ Cu nanoparticles, compared with pure water under same Reynolds number.

Only a limited number of experimental data are available on the heat transfer coefficients of nanofluids in the turbulent flow regime. The experiments lead to the same conclusions as the experiments with laminar flow: the addition of small amounts of nanoparticles to the base-fluid increased the h_c remarkably. For example, some researchers [32, 33, 34] performed experiments which resulted in a significant enhancement of h_c of nanofluids in comparison with the base-fluid. They concluded that the enhancement depends mainly on the Reynolds number and the particles volume concentration. In other words, the maximum heat transfer enhancement in a fully developed flow region takes places with an increase in the Reynolds number and the volume concentration. Contrary with other experimental studies, Sajadi and Kazemi [35] concluded that there was limited effect on the heat transfer enhancement with increasing the volume fraction of nanoparticles. They studied the heat transfer coefficient behavior of titanium dioxide-water nanofluids in a circular pipe for $0.1\% < \phi < 0.25\%$. The results indicated that addition of small amounts of nanoparticles to the base fluid augmented heat transfer coefficient 22% compared with pure water. However, at different concentrations levels, no sensible increase in the heat transfer of nanofluid was obtained. The discrepancy may be due to the volume concentrations used in this experiment are lower than the other researchers, where ϕ varied mostly from 0.5-2%.

D. C. Hernandez Aita Master of Science Thesis

2-2-2 Solid-Gas mixture

Even though many of the studies for heat transfer coefficient are based on solid-liquid suspensions, high h_c of gas-solid suspensions in turbulent channel flows was studied by Pfeffer et.al [30, 36]. His investigations and experiments resulted in two correlations for the h_c with graphite-air nanofluids at atmospheric conditions. Pfeffer based his research on Danzinger's work [37] with spherical glass particles added to air flowing vertically in a glass tube, and Farbar's et.al work [38] with silica-alumina cracking catalyst in vertical transport, among others. Experimental studies for solid-gas mixtures in laminar flow were not found.

All the studies mentioned above concluded that the heat transfer coefficient of nanofluids is significantly higher than that of the base-fluid under the same flow conditions. However, to estimate the enhancement of the h_c for supercritical CO₂ with nanoparticles experiments must be performed. The estimation of the h_c or the thermo-physical properties with correlations obtained in the studies discussed before is inaccurate. Most of the experiments are performed with liquid as base-fluid. Moreover, the correlations for gases are also not good approximations because they are obtained for low pressure and temperature (atmospheric conditions).

2-3 Radiative Properties

Compared to thermal conductivity and convection studies with nanofluids; the radiative properties of nanofluids have received less attention. However, nowadays, the research on radiative heat transfer in nanofluids has been increasing. Mainly because a significant number of studies have revealed that the radiation properties of fluids are expected to enhance greatly in visible wavelengths when nanoparticles are dispersed.

2-3-1 Radiative properties of s-CO₂ as base fluid

There has been much research concerning the radiative properties of carbon dioxide due to its contribution to the greenhouse effect. However, CO_2 molecules absorb sunlight only at specific wavelengths. Figure 2-1 presents the radiation absorption characteristics of carbon dioxide as a function of wavelength at atmospheric conditions. In this Figure, it is shown that the carbon dioxide absorbs sunlight at three specific ranges of wavelengths: in the mid-infrared (with narrow peaks at 2 and 4 μm), and in the far-infrared region (near 15 μm).

Currently, a large amount of data about carbon dioxide is available in several databases, such as HIgh-resolution- TRANsmission (HITRAN), HIgh-TEMPerature (HITEMP) and Carbon-Dioxide-Spectroscopy-Databank (CDSD). However, they do not contain information on the behavior of CO₂ at supercritical conditions. There is very little data found about radiative properties of CO₂ at high pressures and temperatures. Stefani et.al [40, 41] is one of the few researchers that have studied the optical properties of CO₂ at pressures and temperatures higher than atmospheric conditions. His research cover the absorption characteristics of the CO₂ for pressures from 1 to 40 bar and for temperatures from 298 to 600K. The results shown in his work have similar trends than that of the absorption characteristics of the carbon dioxide at atmospheric conditions. The highest peak of absorption in the mid-IR is

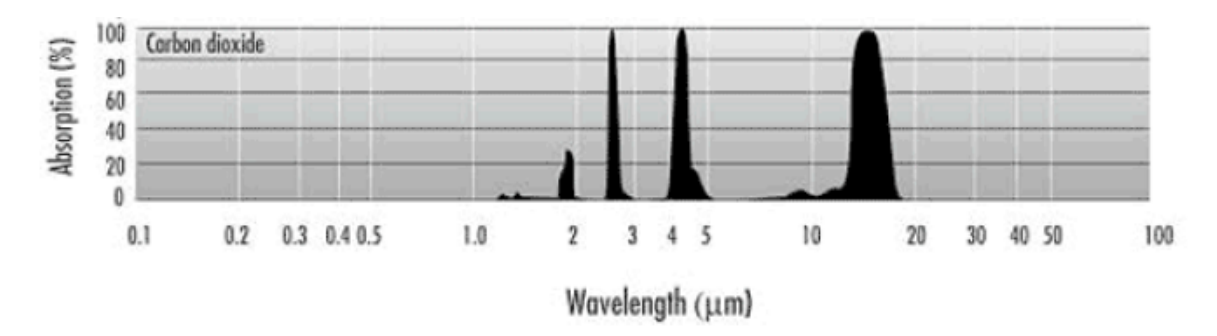


Figure 2-1: Absorption characteristics of Carbon Dioxide at atmospheric conditions [39]

at 2 μm (wavenumber=5000 cm⁻¹) as it is illustrated in Figure 2-2. Therefore, it can be concluded that the CO₂ has very low solar-weighed absorption in this region, due to the short ranges of wavelength where the sunlight is absorbed. For that reason, it is assumed that the carbon dioxide behaves as a transparent fluid to the incoming solar radiation. Therefore, the radiative properties are only tuned via the nanoparticles.

Another important parameter to define the radiative properties of the nanofluid is the refractive index n of the CO_2 . The refractive index determines how much light is bent, or refracted, when entering a material. For most gases the refractive index is very close to unity. For example, air at room temperature has n=1.00029 over the visible spectrum. Therefore, light propagates through gases nearly as fast as through vacuum [42]. n is necessary to estimate the radiative properties of the nanoparticles in the subsection below. Until now, the refractive

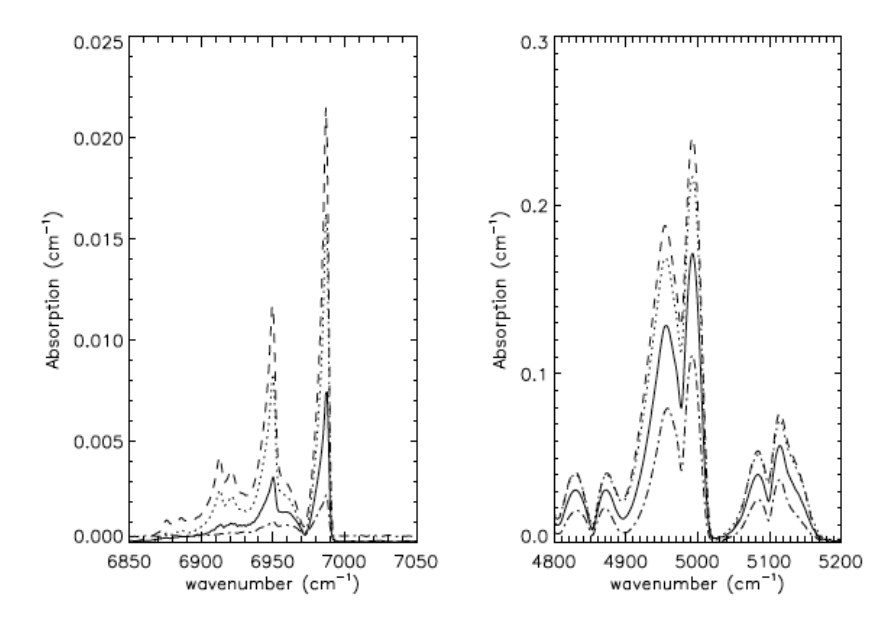


Figure 2-2: CO $_2$ normalized absorption at different pressure and temperature. In the left the spectra at p=1 bar and T=349 K ($dash\ dot$); p=5 bar and T=429K ($black\ curve$); p=15 bar and T=544K (dotted); and p=23 bar and T=583K (dashed). In the right the spectra at p=9 bar and T=502K ($dash\ dot$); p=18 bar and T=563K ($black\ curve$); p=28 bar and T=600k (dotted); and p=32 bar and T=622K (dashed). Each spectrum is acquired with a resolution of 2 cm $^{-1}$ [40]

index of pure CO_2 for supercritical conditions has been measured only by few researchers. Michels and Hamers [43] reported n of carbon dioxide at temperatures between 298 and 373 K and at pressure up to 2400 bar. Adjoury et.al [44] also studied n of CO_2 , but for temperatures between 323 and 373 K and pressures up to 230 bar. Besserer and Robinson [45] presented the effect of temperature and pressure on the refractive index of carbon dioxide for temperatures between 310 and 394 K and pressures up to 102 bar. Figure 2-3 illustrates the behavior of the refractive index for different conditions reported by Besserer and Robinson.

2-3-2 Radiative properties of nanoparticles

When a photon interacts with a medium containing small particles, the radiative intensity may be changed by absorption and/or scattering. How much and into which direction a particle scatters an electromagnetic wave passing through its vicinity depends on three important parameters:

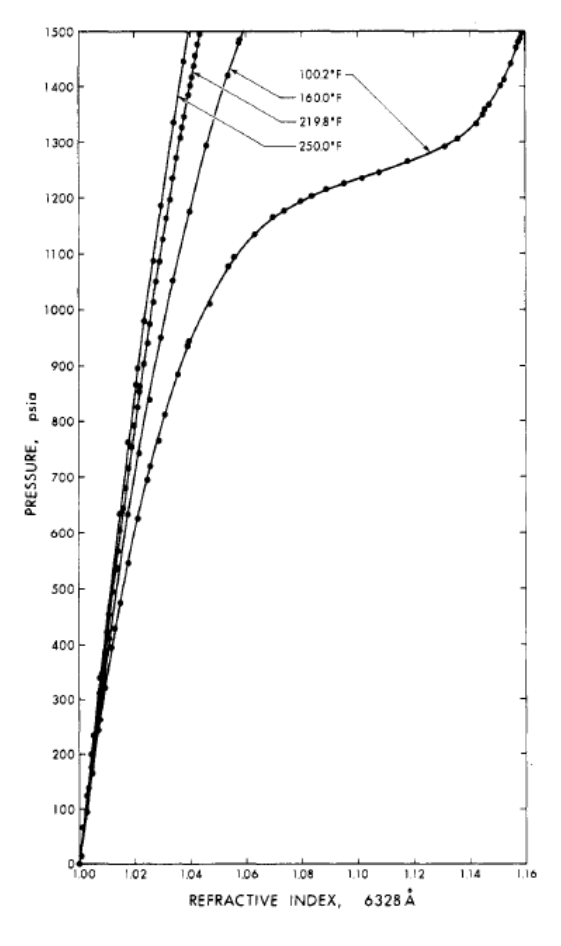


Figure 2-3: Effect of temperature (100.2-250 oF) and pressure (0-1500 psia) on the refractive index of carbon dioxide at $\lambda = 0.6 \mu m$ [45]

1. The shape of the particle:

In radiative analyses the shape of particles is usually assumed to be spherical or cylindrical to simplify the complexity of the calculations. These simplifying assumptions give generally excellent results [42]. Therefore, it will be assumed spherical shape for the nanoparticles.

2. The clearance between particles:

To find the radiative properties of nanoparticles, the approximation of independent scattering is used, which means that scattering by one particle is not affected by the presence of surrounding particles. The approximation can be justified with the used of the classical scattering map illustrates in Figure 2-4. In this Figure, it is shown that nanofluids require low volume concentrations ($\phi < 0.006$) to absorb the incoming solar radiation.

3. Its relative size:

The nanoparticles in volumetric solar receivers are small compared to the wavelength of incident light, which fall into the Rayleigh scattering regime. Equation (2-9) defines the size parameter (α) for the estimation of the extinction coefficient of the nanoparticles.

$$\alpha = \left(\frac{\pi D}{\lambda}\right) << 1 \tag{2-9}$$

The extinction of each particle is the attenuation of an electromagnetic wave by scattering and absorption as it traverses a particulate medium [18]. Based on the independent scattering (ϕ <0.006) and the approximation of the Rayleigh scattering (α <<1), the following relations for the scattering and absorption efficiencies of a spherical particle are used to determine the extinction coefficient [42].

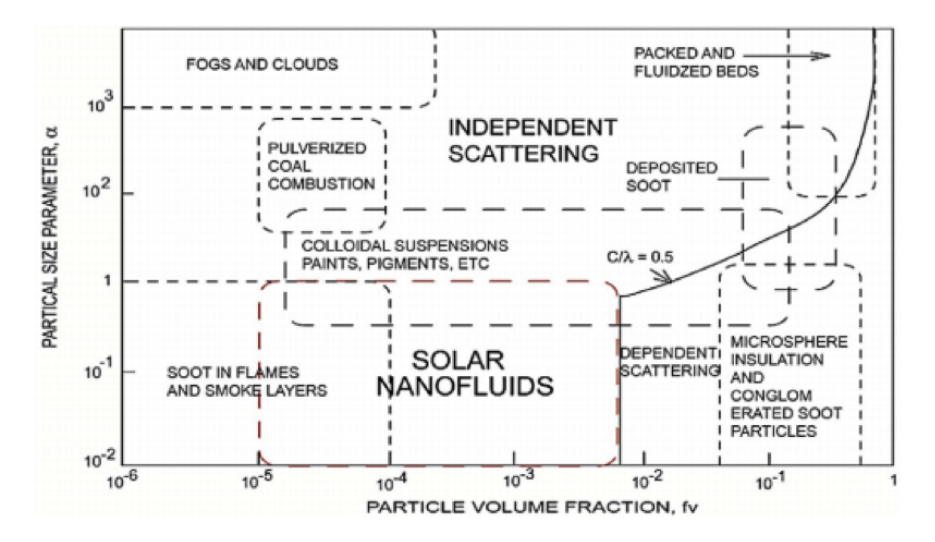


Figure 2-4: Boundary between the independent and the dependent scattering in the scattering regime [46]

$$Q_{scat} = \frac{8}{3}\alpha^4 \left(\frac{m^2 - 1}{m^2 + 2}\right)^2 \tag{2-10}$$

$$Q_{abs} = 4\alpha Im \left\{ \frac{m^2 - 1}{m^2 + 2} \left[1 + \frac{\alpha^2}{15} \left(\frac{m^2 - 1}{m^2 + 2} \right) \frac{m^4 + 27m^2 + 38}{2m^2 + 3} \right] \right\}$$
 (2-11)

$$Q_{ext} = Q_{scat} + Q_{abs} (2-12)$$

Where m is defined as the complex index of refraction of the particle in the fluid medium $(m = (n_p + ik_p)/n_f)$ [42]. n_p is the index of refraction of the particle, k_p the index of absorption of the particle, and n_f the index of refraction of the base-fluid.

The extinction efficiency is simplified for nanoparticles because the higher order terms of the size parameter (α) can be neglected. With this simplification, equations (2-10) and (2-11) show that scattering may be neglected compared with absorption.

The extinction coefficient of the particles is related to the extinction efficiency of each particle (Q_{ext}) by the following equation [42]:

$$\beta_{p,\lambda} = \int_0^\infty Q_{ext} r^2 N(r) dr \tag{2-13}$$

Where r is the ratio of the nanoparticle and N(r) the number density of the particle size. The integral of this equation is related to the volume fraction [42]:

$$\phi = \int_0^\infty \frac{4}{3} \pi r^3 N(r) dr \tag{2-14}$$

Therefore, the extinction coefficient for small particles reduces to:

$$\beta_{p,\lambda} = Im\left(\frac{m^2 - 1}{m^2 + 2}\right) \frac{6\pi\phi}{\lambda} \tag{2-15}$$

Equation (2-15) illustrates that for a given type of particle, the extinction coefficient increases linearly with the increase of the volume fraction.

Finally, the effective extinction coefficient of the nanofluid is equal to the extinction coefficient of the nanoparticles $(\beta_{p,\lambda})$.

$$\beta_{eff,\lambda} = \beta_{p,\lambda} \tag{2-16}$$

Master of Science Thesis

2-4 Optical Thickness

The optical thickness (τ) is the integral of the absorption coefficient along the path (S) on an individual ray of light [42], as defined in equation (2-17):

$$\tau = \int_0^S \beta_{eff,\lambda} \, dS \tag{2-17}$$

It has been observed that with high τ (optically thick), all the incoming light is engrossed in a thin surface layer. Thus, the thermal energy is lost into the environment quite easily. On the other hand, with low τ (optically thin), all the incoming solar radiations are not absorbed [47]. Therefore, an optimum optical thickness τ^{opt} must be calculated in order to improve the design and performance of the volumetric solar receiver.

Chapter 4, shows the optimum optical thickness of the volumetric solar receiver to achieve the highest efficiency of the system. The optical properties of the nanofluid depend on ϕ (equation (2-15)), which means that the optical thickness is dependent on the volume concentration of the particles. By finding τ^{opt} and keeping it constant, the receiver height H can be changed and the optical properties of the nanofluid are adapted to optimum values. Therefore, two important parameters, ϕ and H, are collapsed into a single meaningful parameter, τ^{opt} , in terms of the radiative properties of the nanofluid.

Numerical Modeling of the Volumetric Solar Receiver

A coupled thermal and radiative model is developed to predict the behavior of the volumetric solar receiver. First, the energy balance of the system is discussed. Second, the thermal radiation within the solar collector is described. Third, the boundary conditions of the numerical model are presented. Fourth, the non-dimensional form of the governing equations is defined. Finally, a short description of the numerical method employed is explained.

3-1 **Energy Balance**

The schematic of the volumetric solar receiver is shown in Figure 3-1. The fluid enters the parallel plate configuration, of length L and height H, with a uniform temperature T_{in} , and a velocity u. The nanofluid has a density ρ , a heat capacity C_p , and a thermal conductivity k_c . The incident solar radiation CG_s , where C represents the solar concentration factor and Gsthe incident radiative heat flux, is transmitted through a transparent window, and absorbed volumetrically by the suspended nanoparticles. The absorbed radiation results in a volumetric heat release $q_{gen}^{""}$. The bottom of the volumetric receiver is assumed adiabatic. The convective and radiative losses in the surface of the receiver are considered.

3-1-1 **Simplifications**

The following simplifications are made in order to reduce the complexity of the model:

- Laminar flow is assumed.
- The nanoparticles are assumed to be at the same temperature as the surrounding medium. The high surface area to volume ratio of the particles leads to instant heat transfer to the base-fluid [48].

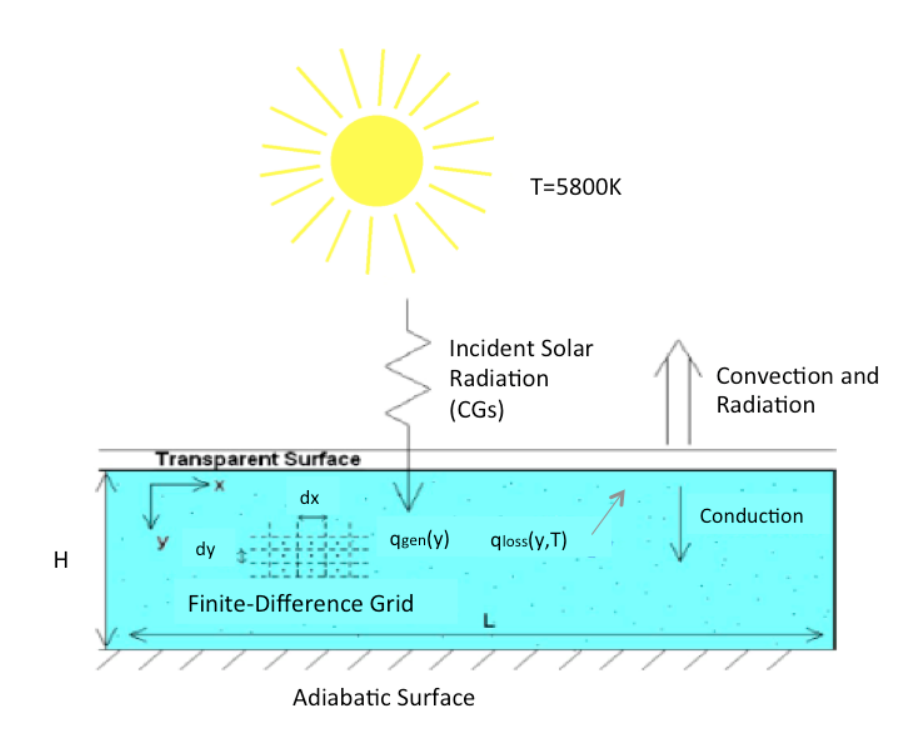


Figure 3-1: 2-D steady-state model of a volumetric solar receiver. Figure adapted from reference [9]

- The nanoparticles are assumed to be uniformly suspended and distributed inside the receiver.
- The thermo-physical properties of the nanofluids are assumed to be the same as the base-fluid. One remarkable feature of nanofluids utilized for energy applications is the enhanced heat transfer due to higher thermal conductivities. The experimental studies, reviewed in chapter 2, describe the enhancement on the thermal properties for $\phi > 0.01$. However, the volume concentration for nanofluid in solar application does not exceed $\phi = 6 \cdot 10^{-3}$ (Figure (2-3)). Therefore, the enhancement in the thermal transport properties is assumed negligible.
- Volumetric solar receivers are assumed to reach high temperatures ($\approx 1000K$) without oxidizing or disintegrating the nanoparticles. Due to the novelty of the subject, experimental data about the oxidation and disintegration of nanoparticles in the base-fluids studied in this thesis have not been found in literature.

3-1-2 Energy Equation

The heat transfer model is considered as a steady-state two-dimensional case. Hence, the energy equation on a differential element inside the nanofluid is given by:

$$\rho u C_p \frac{\partial T}{\partial x} = \frac{\partial}{\partial x} \left(k_c \frac{\partial T}{\partial x} \right) + \frac{\partial}{\partial y} \left(k_c \frac{\partial T}{\partial y} \right) - \nabla q_{rad}$$
 (3-1)

D. C. Hernandez Aita

Master of Science Thesis

3-2 Thermal Radiation 19

where ∇q_{rad} represents the divergence of the radiative heat flux.

3-2 Thermal Radiation

Having discussed the energy equation for the heat transfer process within the receiver, the Radiative Heat Transfer is described in this section to determine the volumetric heat flux (∇q_{rad}) . Some simplifications are made to reduce the complexity of the model:

3-2-1 Simplifications

- Only one interface between the ambient (n_{air}) and the nanofluid $(n_{nanofluid})$ is considered as shown in Figure 3-2. n represents the index of refraction.
- The top surface does not absorb or reflect the solar radiation, CGs, entering the volumetric receiver.
- The bottom of the volumetric receiver is assumed specularly reflective to incident radiation.
- Reflectivity (ρ_r) inside the top surface is assumed zero for angles of reflection below the critical angle $(\delta_c = \arcsin(n_{air}/n_{nanofluid}))$. $\rho_r = 1$ for angles above the critical angle. Figure 3-2 illustrates the angle of refraction (δ) in the volumetric solar receiver.
- Scattering from the nanoparticles is neglected compared with absorption as seen in chapter 2. Therefore, the spectral extinction coefficient (β_{λ}) for nanofluids is equal to the absorption coefficient (k_{λ}) .

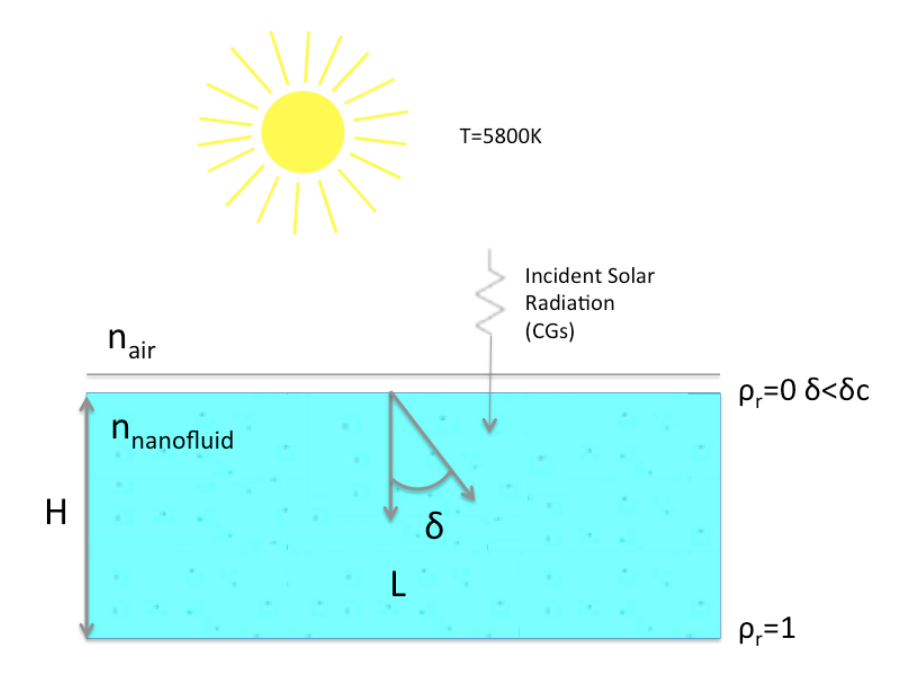


Figure 3-2: Angle of refraction in the volumetric solar receiver

- The nanofluid is assumed as a gray medium [10]. Hence, the extinction coefficient is equal for all wavelengths $(\beta_{\lambda} \approx \beta)$.
- The radiative properties of the nanofluid are assumed temperature independent. This assumption is made to simplify the analysis and due to the lack of reliable data.

3-2-2 Radiative Transfer Equation (RTE)

Under the approximations made above, the Radiative Transfer Equation, along a certain path s, is given by [42].

$$\frac{dI_{\lambda}}{ds} = \beta(I_{bb,\lambda} - I_{\lambda}) \tag{3-2}$$

Equation (3-2) simultaneously describes how the spectral intensity exponentially decays due to absorption (I_{λ}) and is augmented due to thermal re-emission at high temperatures ($I_{bb,\lambda}$).

The solution to the equation (3-2) is given by [42].

$$I_{\lambda}(s) = I_{\lambda}(0)e^{-\beta * s} + I_{bb,\lambda}(1 - e^{-\beta * s})$$
 (3-3)

The RTE applies for each wavelength, and for each direction of ballistic transport. In order to determine the volumetric heat flux within the receiver, the spectral intensity must be integrated over the entire spectrum and over all directions, and then differentiated with respect of y [42].

$$\nabla q_{rad} = \frac{d}{dy} \int_0^{2\pi} \int_0^{\infty} \int_0^{\pi/2} I_{\lambda}(y) cos\theta sin\theta \, d\theta \, d\lambda \, d\psi$$
 (3-4)

 ∇q_{rad} results in a volumetric heating from the incident solar radiation $(q_{gen}^{""}(y))$ and a volumetric heat loss because of thermal re-radiation from the nanofluid at high temperatures $(q_{loss}^{""}(y,T))$ (see Figure 3-1):

$$-\nabla q_{rad} = +q_{qen}^{""}(y) - q_{loss}^{""}(y,T)$$
 (3-5)

Considering that the solar and thermal radiation spectrums are broadband, simplifications need to be done to reduce the number of equations. To simplify the analysis, the whole spectrum is divided into two regions ($Band~I~(\lambda < 2\mu m)$ and $Band~II~(\lambda > 2\mu m)$) as illustrated in Figure 3-3. The solid line represents the distribution of the concentrated solar irradiation, which is modeled only in Band I because approximately 95% of the Sun is absorbed in this region. On the other hand, the dotted-dashed and dashed lines represent the thermal emission of the volumetric receiver at different temperatures (900 K and 1200 K). The thermal emission is modeled separately in the two regions. In the spectral Band I, the thermal emission or radiative loss is captured using the RTE (Equation (3-3)). In the spectral Band II, the radiative loss is estimated using the boundary condition at the top surface of the receiver. This treatment is based on the assumption that most of the thermal radiation occurs in Band II, where the nanofluid can be modeled either as optically thick $(\tau \to \infty)$, or as optically thin $(\tau \to 0)$ depending on the base-fluid.

D. C. Hernandez Aita

3-2 Thermal Radiation 21

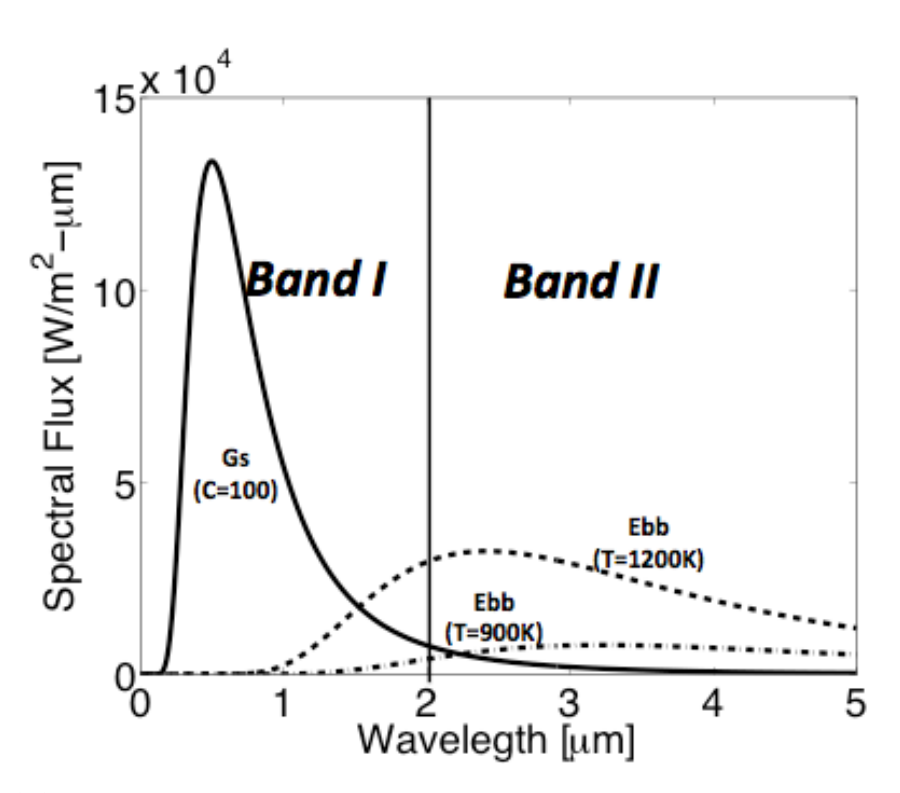


Figure 3-3: Distribution of concentrated solar irradiation and of a black body thermal emission

3-2-3 RTE Solving Methodology

The methodology to solve the Radiative Transfer Equation is illustrated in Figure 3-4. The RTE is divided in Band I and Band II. In Band I, the volumetric heat flux is separated in two different equations. The absorption of the incident solar radiation by the nanoparticles $q_{loss}^{""}(y)$, and the diffuse thermal re-radiation from the nanofluid at high temperatures $q_{loss}^{""}(y,T)$. This methodology has been implemented because $q_{loss}^{""}(y,T)$, which represents the thermal re-emission term $I_{bb,\lambda}$ in equation (3-2), is a strong function of the temperature, which complicates the solution. While $q_{gen}^{""}(y)$, which represents the absorption term I_{λ} in equation (3-2), only depends on the y direction. In Band II, two cases may be considered. The base-fluid is a blackbody, or the base-fluid is considered transparent.

3-2-4 Band I

The following sub-sections explain how the RTE is solved for the incoming solar radiation and for the thermal re-radiation for wavelengths between 0-2 μm .

Volumetric Heat Generated

Solving the RTE for the incident solar radiation is essential to the model because it dictates the distribution of the volumetric heat generated inside the receiver. For this case, equation (3-3) can be explicitly solved and then incorporated into the energy equation. Equation (3-4) is simplified because solar radiation can be approximately treated as a collimated light source

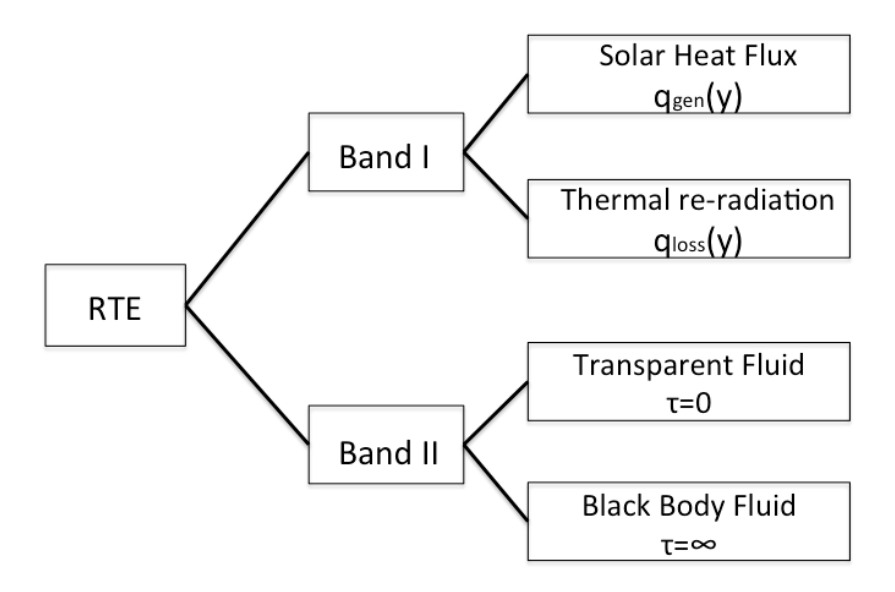


Figure 3-4: RTE distribution in Band I and Band II

owing to its small angle of incidence [42]. Therefore, the volumetric heat generated can be written as:

$$q_{gen}^{"'} = \frac{d}{dy} \int_0^{2\mu m} I_{\lambda}(y) \, d\lambda \tag{3-6}$$

Passes Within The Receiver. Depending on the volume fraction of the nanoparticles, the incident solar radiation could be attenuated in one-pass, or in two-passes of the receiver (utilizing the ideal reflector at the bottom wall y=H). Figure 3-5 illustrates in a solid line the cumulating volumetric heat generated for both cases. When the two profiles are compared, it is clear that for two-passes (Figure 3-5(b)), the incident solar radiation results in a more uniform distribution of $q_{gen}^{"'}$ inside the receiver. In this case, all the nanoparticles contribute to the heat transfer process. For one-pass (Figure 3-5(a)), the $q_{gen}^{"'}$ becomes almost zero for the bottom half of the receiver, which is not desired. Therefore, in this work, the incident solar radiation is attenuated within two-passes of the receiver. Thus, two boundary conditions of the RTE are required for solving the volumetric heat generated: one at the top surface (I_{λ}^+) and one at the bottom surface of the receiver (I_{λ}^-) .

The boundary conditions of the RTE are:

$$I_{\lambda}^{+} = S_{att} C \Omega_s I_{bb,\lambda}(T_{sun}) \tag{3-7}$$

$$I_{\lambda}^{-} = I_{\lambda}^{+} e^{-H\beta} \tag{3-8}$$

where T_{sun} is the sun's temperature (5800 K), Ω_s (6.8x10⁻⁵) is the solid angle of the sun as seen from Earth, and S_{att} (0.73) is the attenuation constant [42].

3-2 Thermal Radiation 23

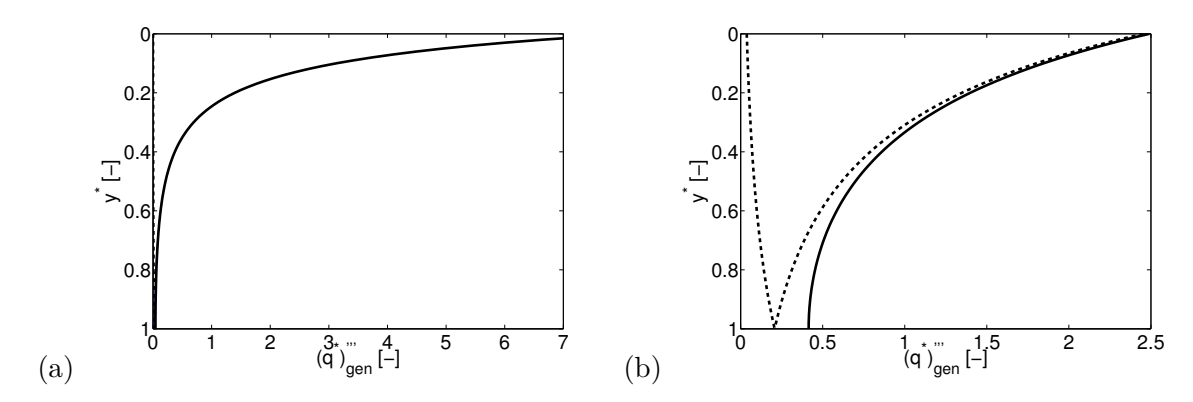


Figure 3-5: Cumulating volumetric heat generated (—) for one-pass (a) and two-passes (b). Volumetric heat generated in each pass (- - -).

The concentrated (normally-incident) solar radiation is approximated using the Planck's black body radiation $(I_{bb,\lambda})$ [42]:

$$I_{bb,\lambda}(T) = \frac{2hc^2}{\lambda^5} \frac{1}{e^{hc/\lambda T k_b} - 1}$$
(3-9)

where h (6.626x10⁻³⁴ Js) is the Plank's constant, c (2.99x10⁸ m/s) the speed of light, T the temperature, and k_b (1.38x10⁻²³ J/K) the Boltzmann constant.

The decay of intensity due to absorption is given by:

$$I_{\lambda(1)}(y) = I_{\lambda}^{+}(e^{-\beta * y} + e^{-\beta * (2H - y)})$$
(3-10)

Finally, equation (3-10) is integrated for wavelengths between 0-2 μm , and then differentiated along the y direction to obtain the volumetric heat generated $(q_{gen}^{"'})$:

$$q_{gen}^{""} = \frac{d}{dy} \int_0^{2\mu m} I_{\lambda}^+ (e^{-\beta * y} + e^{-\beta(2H - y)}) d\lambda$$
 (3-11)

Volumetric Heat loss due to re-radiation:

In order to solve the RTE (equation (3-3)) for the thermal re-radiation within the volumetric receiver, the knowledge of the temperature profile is required. However, the temperature profile is unknown until the energy equation is solved. Therefore, these two equations need to be solved simultaneously.

The volumetric re-radiation problem only becomes important as the temperature exceeds 1000K as illustrated in Figure 3-6 . However, it is not until the temperature reaches $\approx 1400~\mathrm{K}$ that the heat loss inside the receiver begins to dominate. Nonetheless, it is usually undesirable to operate at temperatures higher than 1400 K because the material of the nanoparticles and their stability in the nanofluid is questionable at these temperatures.

The same approach used to solve the incident solar radiation (two-passes within the receiver) is presented in this case. The gain of intensity due to emission is given by:

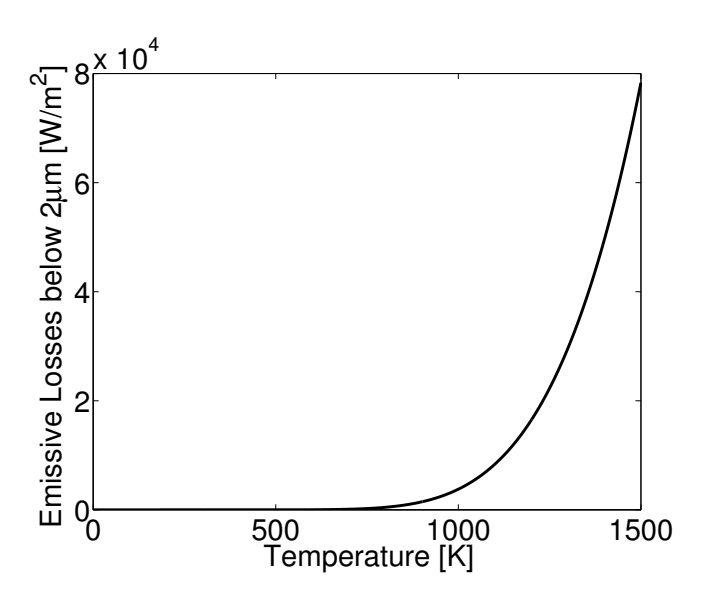


Figure 3-6: Thermal Re-radiation as function of temperature

$$I_{\lambda(2)}(y,T) = I_{bb,\lambda}(T)((1 - e^{-\beta * y}) + (1 - e^{-\beta(2H - y)}))$$
(3-12)

Thermal re-radiation is treated as a volumetric heat loss, governed by equation:

$$q_{loss}^{""} = 2E_1(T)\beta \int_0^{\delta_c} \left(e^{-\frac{\beta(2H-y)}{\cos\theta}} + e^{-\frac{\beta y}{\cos\theta}}\right) \cos\theta \sin\theta \, d\theta \tag{3-13}$$

Where the emissive loss in the Band I is defined as:

$$E_1(T) = \pi \int_0^{2\mu m} I_{bb,\lambda} d\lambda \tag{3-14}$$

Equation (3-13) cannot be explicitly solved due to the dependency on temperature. Thus, the inclusion of the term in the numerical model is very time-consuming and only provides changes in the solutions for very high temperatures. Therefore, the radiative heat loss within the receiver is not incorporated in the numerical model for the results presented in chapter 4.

3-2-5 Band II

In the spectrum Band II, it is assumed that only the base-fluid absorbs and emits in the IR region. As explained previously, the nanofluid can be modeled either as optically thick $(\tau \to \infty)$, or as optically thin $(\tau \to 0)$ depending on the base-fluid. In the case of modeling the nanofluid as optically thick, the base-fluid is considered a black body radiator $(\epsilon = 1)$ owing to the inherntly high absorption coefficient of the heat transfer fluid in the mid-infrared wavelength band. In the case of modeling the nanofluid as optically thin, the base-fluid is considered transparent $(\epsilon = 0)$ due to the low absorption coefficient in the mid-infrared.

The emissive loss in the Band II is defined as:

$$E_2(T) = \pi \int_{2\mu m}^{\infty} I_{bb,\lambda} \, d\lambda \tag{3-15}$$

3-3 Boundary Conditions

In this analysis, the boundary conditions of the volumetric solar receiver are:

$$T|_{x=0} = T_{in} (3-16)$$

$$\left. \frac{\partial T}{\partial y} \right|_{y=H} = 0 \tag{3-17}$$

$$k_c \frac{\partial T}{\partial y}\Big|_{y=0} = h_c(T_{y=0} - T_{amb}) + \epsilon \left(E_2(T_{y=0}) - \sigma T^4_{amb}\right)$$
(3-18)

where h_c represents the heat transfer coefficient, ϵ the emissivity, σ (5.67x10⁻⁸ W/m²K⁴) the Stefan-Boltzmann constant, T_{amb} (25 oC) the ambient temperature , and $E_2(T_{y=0})$ the emissive loss in Band II.

3-4 Non-dimensional Form

The non-dimensional form of the energy equation and boundary conditions are obtained by substituting the following **dimensionless variables** in equations (3-1) and (3-16)-(3-18):

$$\theta = \frac{T}{T_{in}}; \qquad \theta_{amb} = \frac{T_{amb}}{T_{in}};$$

$$x^* = \frac{x}{H}; \qquad y^* = \frac{y}{H} \qquad u^* = \frac{u}{u_0};$$

$$\rho^* = \frac{\rho}{\rho_0}; \qquad C_p^* = \frac{C_p}{C_{p0}}; \qquad k_c^* = \frac{k_c}{k_{c0}}; \qquad h^* = \frac{h}{h_0};$$

$$(q^*)_{gen}^{"''}(y^*) = \frac{q_{gen}^{"''}(y)H}{CG_s}; \qquad (q^*)_{loss}^{"''}(y^*, \theta) = \frac{q_{loss}^{"''}(y, T)H}{CG_s}; \qquad R = \frac{CG_sH}{T_{in}k_{c0}};$$

$$Pe = RePr = \frac{\rho_0 u_0 C_{p0}H}{k_{c0}}; \qquad Nu = \frac{h_cH}{k_{c0}}; \qquad Sf = \epsilon \frac{\sigma H T_{in}^3}{k_{c0}};$$

where, the subscript 0 refers to the inlet condition, Nu is the Nusselt number, Re the Reynolds number, Pr the Prandtl number, Pe the Peclet number and Sf the Stefan number. R is a dimensionless number which represents the ratio of the heat transferred by the incident solar radiation to that transferred by conduction.

Substituting the variables above in equation (3-1), the **non-dimensional energy equation** becomes:

$$Pe\rho^*u^*Cp^*\frac{\partial\theta}{\partial x^*} = \frac{\partial}{\partial y^*}\left(k_c^*\frac{\partial\theta}{\partial y^*}\right) + \frac{\partial}{\partial x^*}\left(k_c^*\frac{\partial\theta}{\partial x^*}\right) + (q^*)_{gen}^{""}(y^*)R - (q^*)_{loss}^{""}(y^*,\theta)R \quad (3-20)$$

The **boundary conditions** of the volumetric receiver becomes:

$$\theta|_{x^*=0} = 1 \tag{3-21}$$

$$\left. \frac{\partial \theta}{\partial y^*} \right|_{y^* = H} = 0 \tag{3-22}$$

$$\left. \frac{\partial \theta}{\partial y^*} \right|_{y^*=0} = Nu(\theta_{y^*=0} - \theta_{amb}) + St \left(\frac{E_2(\theta_{y^*=0})}{\sigma T_{in}^4} - \theta_{amb}^4 \right)$$
(3-23)

where Nusselt number represents the ratio of convective to conductive heat transfer across the boundary, and the Stefan Number [49] expresses the ratio of the heat transferred by radiation to that transferred by conduction.

3-5 Numerical Method

The numerical method is implemented using a *MATLAB* code [50] to obtain the solution of the two-dimensional steady state model.

Finite difference technique has been applied to numerically solve the energy equation. The advection term has been approximated with a first-order derivative, while the diffusion terms have been approximated with a central difference second-order derivative. The spatial directions, in x and y, were divided into uniform nodes of N_x and N_y points, respectively.

A steady state solver was used because of a faster convergence rate as compared to an unsteady solver. The solution obtained using both steady and unsteady solvers were found to be the same. The steady state solver is obtained by keeping the diffusive and advection terms that change in the y-direction at a new iteration level, and obtaining the other terms from the previous iteration.

Previous studies have revealed that nanofluid-based volumetric receivers are an efficient method of capturing concentrated solar radiation. However, the benefits of this type of receiver with supercritical carbon dioxide, as a base-fluid, have not been studied in the past. The purpose of this chapter is to use the model developed in chapter 3 to propose design guidelines of a volumetric solar receiver with s-CO₂ and carbon nanoparticles as working fluid. These results aim to provide helpful starting point for future research in the development of volumetric solar receivers for the s-CO₂ Brayton cycle in solar applications.

The chapter begins with a brief description of the receiver efficiency and the overall system efficiency. Later on, a comparison of Therminol VP-1 and s-CO₂ as the base-fluid of volumetric solar receivers is presented. In this section, a parameter study to understand the influence of the optical thickness τ , the receiver height H and the solar concentration factor C on the efficiency of the system is presented. Furthermore, in order to assess the potential of volumetric absorption systems as efficient solar energy harvesters, these are compared to surface-based systems using both base-fluids. The last part of this chapter focuses on the volumetric solar receiver for the s-CO₂ Brayton cycle. In this section, a comparative analysis of the solar collector with low and high inlet temperature is presented.

4-1 System Performance

4-1-1 Receiver Efficiency

The efficiency of a solar thermal receiver is the ratio of the collected thermal energy to the total incident energy, as defined by equation (4-1).

$$\eta_{rec} = \frac{\dot{m}(h_{out} - h_{in})}{Q_{in}A_{rec}} = \frac{k_{c0}Peh_{in}(h_{out}^* - 1)}{Cp_0Q_{in}H_{rec}L_{rec}^*}$$
(4-1)

The right expression represents the efficiency of the receiver in terms of non-dimensional variables described in Chapter 3. L_{rec}^* represents the dimensionless length of the receiver

 $(L_{rec}^* = L_{rec}/H_{rec})$, k_{c0} , and Cp_0 are the properties at inlet condition, Pe is the Peclet number, Q_{in} is the solar heat flux entering the receiver and h is the enthalpy.

4-1-2 Overall System Efficiency

In power generation applications, where the volumetric solar receiver will be coupled to a power generation cycle, the total efficiency of the system will be a product of the receiver efficiency and the power generation cycle efficiency. In an ideal case, the power generation efficiency can be approximated by the Carnot efficiency, as defined by equation (4-2).

$$\eta_{carnot} = 1 - \frac{T_{amb}}{T_{out}} = 1 - \frac{\theta_{amb}}{\theta_{out}} \tag{4-2}$$

Therefore, the total efficiency can be expressed as:

$$\eta_{sys} = \eta_{carnot}\eta_{rec} \tag{4-3}$$

4-2 Comparison of Therminol VP-1 and s-CO₂ as the base-fluid of a Volumetric Solar Receiver

Therminol VP-1 (eutectic mixture of diphenyl oxide and biphenyl) is a commonly used heat transfer fluid in solar applications, especially in parabolic trough power plants. A comparative analysis between this oil and s-CO₂ is performed. To compare both fluids, the input parameters of the volumetric solar receiver model are set to:

- H=2.5 cm;
- C=10;
- Gs= 1000 W/m^2 ;
- T_{in} =400 K;
- Nu=1;
- Re=1500.

Assumptions

Due to the nature of each fluid, some particular assumptions have to be made:

- 1. Thermo-physical Properties:
 - VP-1: The properties are independent of temperature. The thermo-physical properties of Therminol VP-1 do not vary considerably [10], which makes the assumption of constant properties applicable for this study case.

• s-CO₂: Two cases are studied. a) The properties are independent of temperature. b) The properties are dependent on temperature. For the second case, a thermodynamic library called Fluidprop [51] was used for the calculation of k_c , ρ , Cp, μ . Figure 4-1 illustrates the properties as function of the temperature.

The following values represent the thermo-physical properties of both fluids used in the numerical model of the volumetric solar receiver. In the numerical model with s-CO₂ with constant properties, k_c , ρ , Cp, μ are average values of the thermo-physical properties estimated by Fluidprop from T=400K to T=1100K at $P_0=250bar$. In the numerical model with variable properties, these values are calculated at the inlet condition of the receiver, and used to compute the dimensionless variables $\rho*$, k_c* and Cp* in the energy equation.

Constant Properties:

Therminol VP-1:

- k_{c0} =0.1357 W/m K;
- $\rho_0 = 1060 \text{ kg/m}^3$;
- $Cp_0=1570 \text{ J/kg K};$
- $\mu_0 = 2.628 \times 10^{-3} \text{ Pa·s};$
- Pr=30.414;
- $Pe=4.562 \times 10^4$.

Supercritical CO₂:

- k_{c0} =0.061 W/m K;
- $\rho_0 = 208.14 \text{ kg/m}^3$;
- $Cp_0=1334 \text{ J/kg K};$
- $\mu_0 = 3.707 \times 10^{-5} \text{ Pa·s};$
- Pr=0.811;
- $Pe=1.226 \times 10^3$.

Variable Properties:

Supercritical CO₂:

- k_{c0} =0.055 W/m K;
- $\rho_0 = 481.59 \text{ kg/m}^3$;
- $Cp_0=1962.31 \text{ J/kg K};$
- $\mu_0 = 3.85 \times 10^{-5} \text{ Pa·s};$
- $h_0 = 4.605 \times 10^5 \text{ J/kg}$;
- Pr=1.360;
- $Pe=2.040x10^3$.

2. Velocity:

• VP-1: A plug flow velocity profile is assumed in the modeling of the nanofluid-based volumetric receivers with constant properties [52].

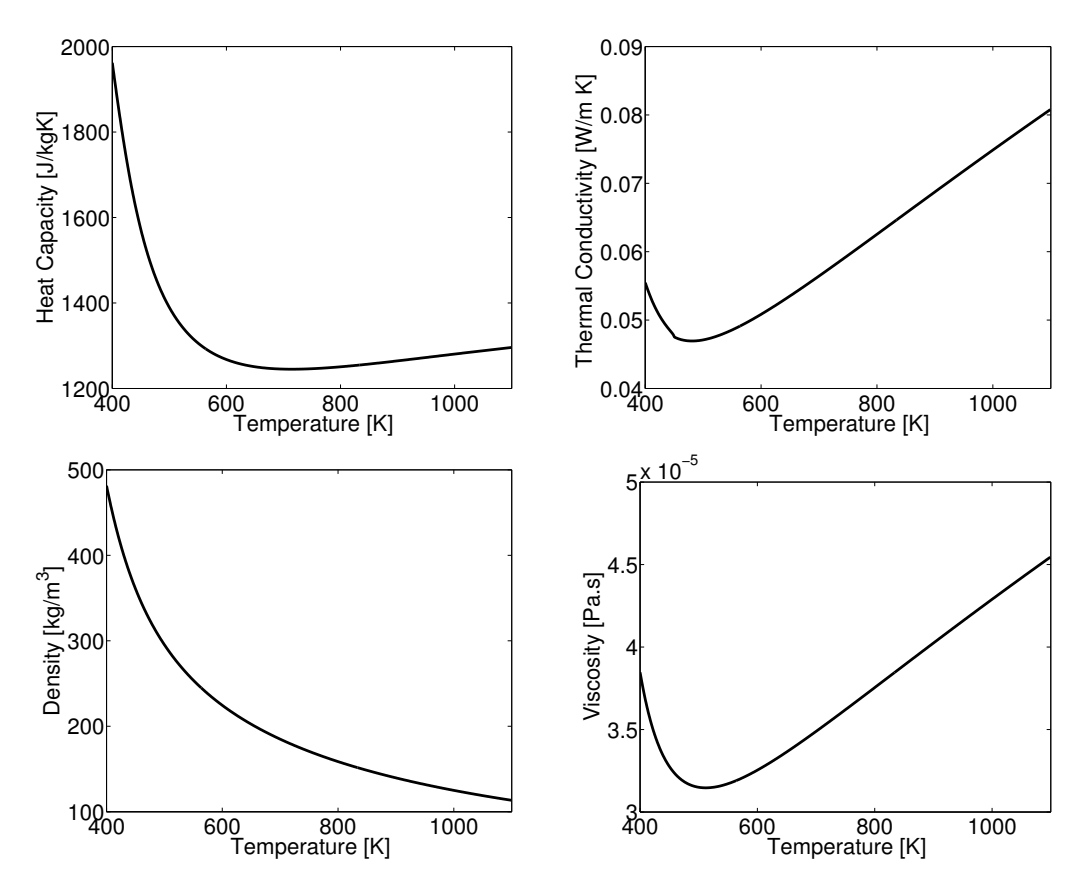


Figure 4-1: Properties of s-CO $_2$ as function of temperature at P $_0$ =250 bar

• s-CO₂: a) A plug flow velocity profile is also assumed for the case of constant properties. b) A plug flow velocity profile for each node in the x-direction is assumed in the case of variable properties. Using the mass conservation equation $(\int_0^1 \rho U dy = 1)$ and taking U as constant in each cell in the x-direction, the plug flow formulation $(U(x) = \frac{1}{\int_0^1 \rho dy})$ was achieved.

3. Optical Thickness:

The optimum value of optical thickness, τ , depends on the radiative properties of each nanofluid. The index of refraction of Therminol VP-1 is set to $n_p=1.63$ [52], while the index of refraction of supercritical carbon dioxide is fixed to $n_p=1.11$ [43]. The radiative properties of the carbon nanoparticles are fixed to $n_f=2.72$ and $k_f=1.31$ [52]. In the sub-section 4-2-1 (parameter analysis) the procedure to calculate the τ^{opt} for each base fluid is explained.

- VP-1: $\tau^{opt} = 1.2$
- s-CO₂: $\tau^{opt} = 1.6$

4. Emissivity:

• VP-1: $\epsilon = 1$. The nanofluid with Therminol VP-1, as base-fluid, is modeled as fully absorptive (black body) for the spectral Band II (see Chapter 3). The broad

vibrational and rotational absorption bands of the liquid are assumed to overlap and dominate in the infrared region [10].

• s-CO₂: $\epsilon = 0$. The nanofluid with s-CO₂, as base-fluid, is modeled as a transparent fluid for the spectral Band II. The absorption characteristics of carbon dioxide are poor in the mid-infrared region, as documented in chapter 2.

Temperature Profile

The temperature profiles for both VP-1 and s-CO₂ models are shown in Figure 4-2. The transverse temperature profile at different axial locations of a 2.5cm receiver height with 10 suns of incident solar radiation ($CGs=10 \ kW/m^2$) is illustrated in Figure 4-2 (a). The axial temperature at the top and bottom surfaces and at the middle of the receiver is sketched in Figure 4-2 (b). Figure 4-3 shows the two-dimensional temperature contour within the volumetric solar receiver.

The comparison between both nanofluids presents interesting numerical results. Firstly, the dimensionless receiver length L_{rec}^* in the study case with Therminol VP-1 is considerably longer than in the study case with s-CO₂. The difference in L_{rec}^* is caused by a higher Pe number for Therminol VP-1 (one order of magnitude larger) than for s-CO₂. The Reynolds number is fixed to 1500, however, the Prandl number is approximately 30 times higher for the synthetic oil than for supercritical carbon dioxide, resulting in larger Pe number.

Secondly, higher temperatures inside the receiver are reached in the volumetric solar receiver with s-CO₂ as base fluid. The result is caused because of difference in the heat loss from the top surface to the surroundings. As it was explained previously, s-CO₂ has been modeled as transparent fluid without emissive loss in the Band II. This assumption results in only convective loss in the numerical model. However, in the case of Therminol VP-1, as base-fluid, both emissive and convection losses from the top surface to the surroundings are considered. Therefore, larger heat losses result in lower outlet temperature of the solar collector with Therminol VP-1.

Finally, the temperature profile within the volumetric solar receiver with s- CO_2 illustrates the effect of using constant (black color) and variable (red color) properties in the model. It is observed that if the thermo-physical properties of the volumetric receiver are kept constant, greater temperatures are predicted. Therefore, assuming constant properties in the volumetric solar receiver with s- CO_2 overestimated the temperature profile.

Receiver Performance

The numerical model shows greater system performance with s-CO₂ than with Therminol VP-1, as illustrated in Figure 4-4. The lack of emissive loss to the surroundings in the volumetric solar receiver with s-CO₂ improves considerably the receiver performance, leading to approximately 20% higher efficiency of the system compared with Therminol VP-1.

The temperature profile is shown for different positions of x^* . However, the length of the receiver should be optimized to reduce unnecessary cost and footprint. The opposing trends of the receiver efficiency and the Carnot efficiency with increasing temperature gives rise to an optimum system efficiency η_{sys}^{opt} . The optimum system efficiency has an specific length of the

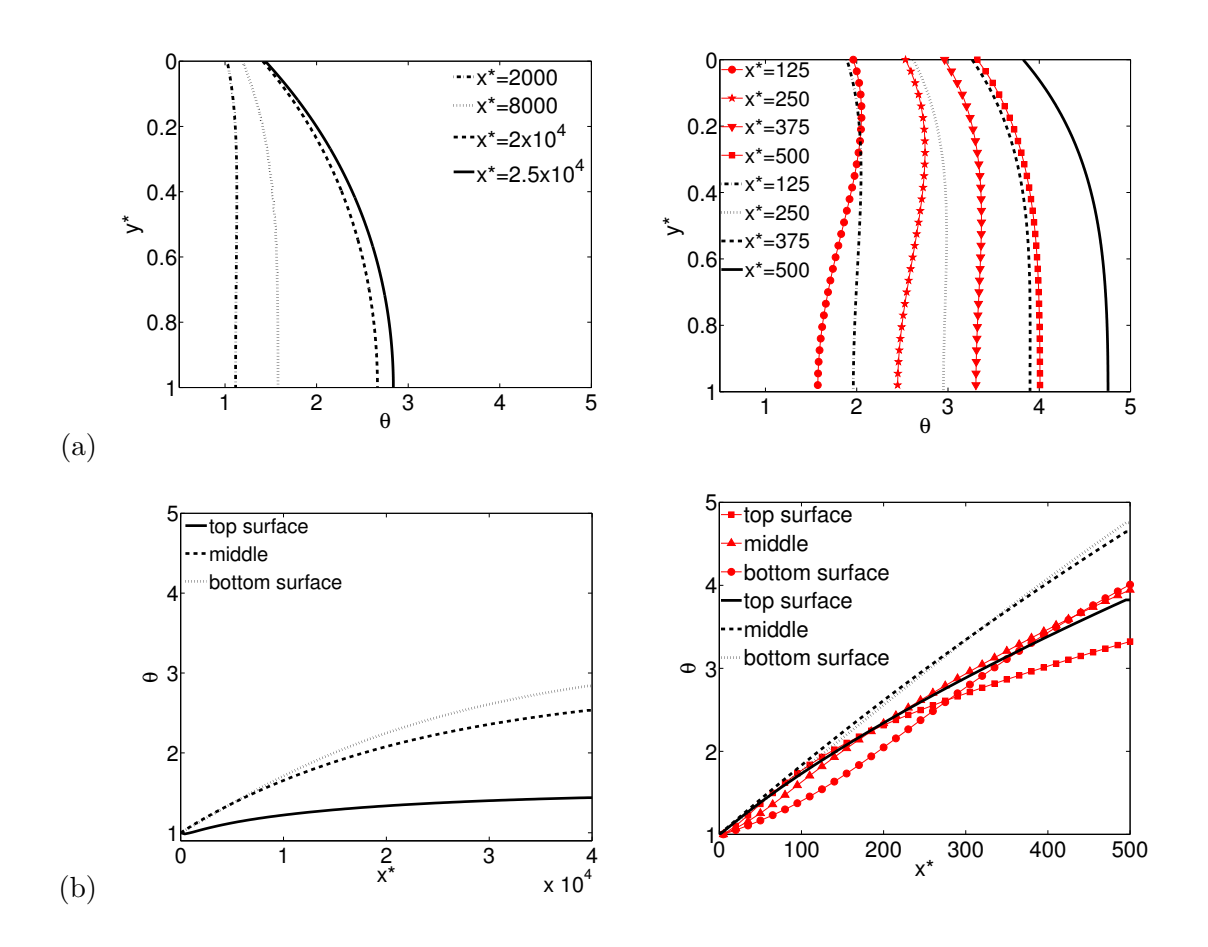


Figure 4-2: VP-1 (left column) and s-CO $_2$ (right column). (a) Transverse temperature profile at different axial locations. (b) Axial temperature profile at the top, middle and bottom of the receiver. Constant properties in *black* and variable properties in *red*.

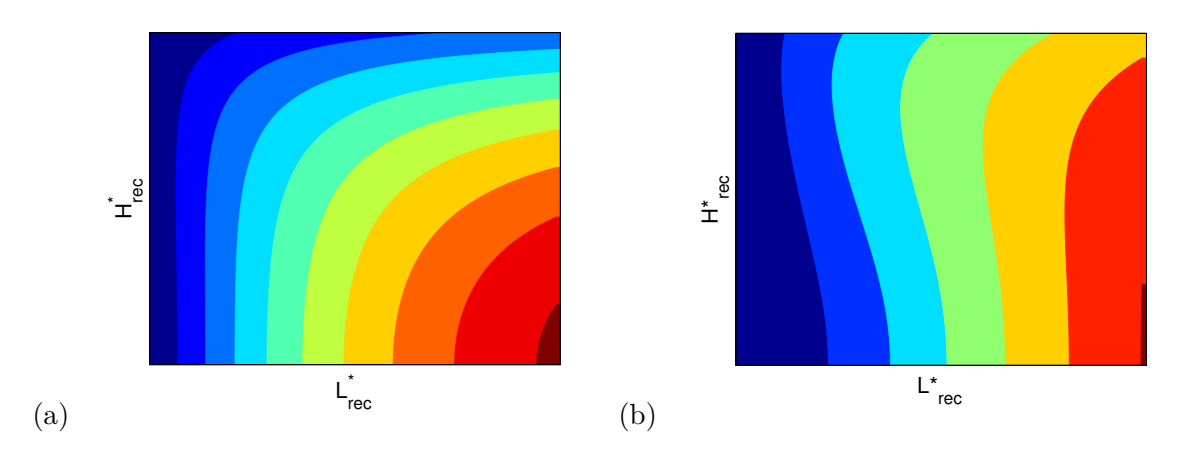


Figure 4-3: Temperature contour within the volumetric receiver. (a) Therminol VP-1. (b) s-CO $_2$ with variable properties.

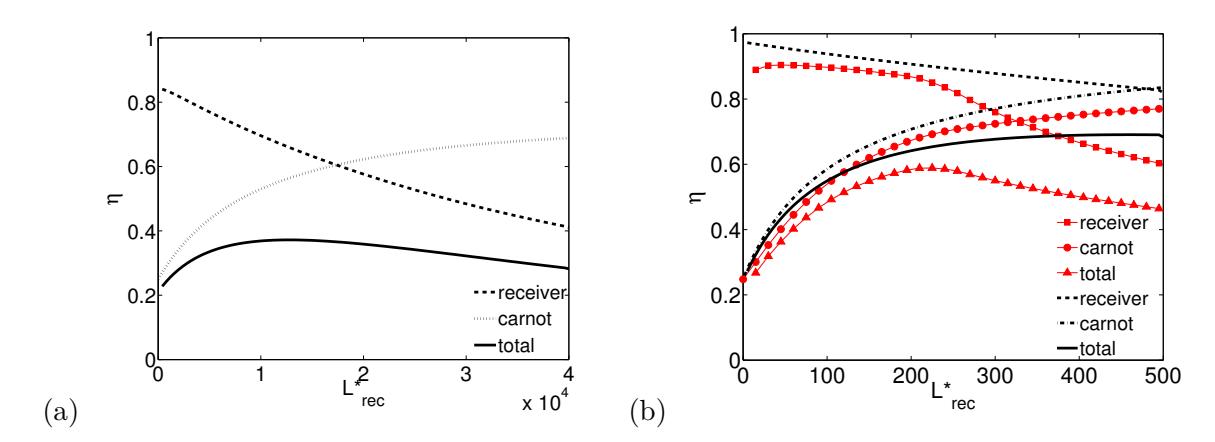


Figure 4-4: Receiver, carnot and system efficiencies as function of the dimensionless receiver lenght. (a) Therminol VP-1. (b) s-CO $_2$. Constant properties in *black* and variable properties in *red*.

receiver L_{rec}^* that can be used as starting point for the design of the volumetric solar receiver. In the case with Therminol VP-1, L_{rec}^* is approximately $1.3\cdot 10^4$ to achieve a $\eta_{sys}^{opt} \approx 38\%$. In the volumetric receiver with s-CO₂ with variable properties, L_{rec}^* is approximately 220 to obtain a $\eta_{sys}^{opt} \approx 58\%$. However in the case with s-CO₂ with constant properties, L_{rec}^* is approximately 500 to reach a $\eta_{sys}^{opt} \approx 68\%$, which means that the effect of the variation of the properties not only increases the temperature within the receiver, but also overestimated the performance and design of the volumetric receiver.

In the study case with Therminol VP-1, the optimum system efficiency is achieved at a $\theta_{out}^{opt} = 1.72$, which corresponds to an outlet temperature of 415.5°C. However, this temperature is greater than the breakdown temperature of this oil (T_{max} =400°C [53]). Therefore, the optimum system efficiency cannot be reached for these operating conditions using Therminol VP-1. To lower the outlet temperature, the length of the receiver has to be reduced. In the case with s-CO₂ with variable properties, the optimum temperature outlet is 673°C ($\theta_{out}^{opt} = 2.4$), which is physically feasible for this fluid. After the comparative analysis between both fluids, it is clear that an optimization of the volumetric solar receiver can be performed by replacing the base-fluid of the nanofluid from Therminol VP-1 to s-CO₂. Supercritical carbon dioxide achieves better efficiencies, and works at higher temperatures than Therminol VP-1. Moreover, it reduces the sizes of the receiver. Other important advantages of this supercritical fluid were summarized in chapter 1.

4-2-1 Parameter Analysis

A parameter analysis is performed to study the potential improvement of the system efficiency by varying specific inputs of the receiver design. The methodology followed in this analysis is that the parameter whose effect is to be investigated is varied, while all other parameters are held constant. Subsequently, the overall system efficiency, η_{sys} , is calculated for each value of that parameter. Three important cases are presented. First, the effect of the optical thickness τ is examined. Second, the effect of the receiver height H is studied. Finally, the effect of

the solar concentration factor C is investigated. In order to understand the behavior of the η_{sys} for different configurations of the receiver, the parameters that have an influence on τ and η_{sys} are presented below:

- $\tau = f(H, \phi, n_p, k_p, n_f)$. The radiative properties of the nanofluid, n_p, k_p, n_f , are constant due to the assumption made in chapter 3 of gray medium;
- $\eta_{sys} = f(\tau, H, C, T_{in}, k_{0c}, \rho_0, Cp_0).$

Effect of Optical Thickness

The optical thickness of a volumetric solar receiver can be adjusted by varying the volume fraction of the nanoparticles (equation (2-17)) for a given receiver height. With increasing optical thickness, all the incoming light is engrossed in a thin surface layer, which makes the volumetric receiver behaves more closely as a surface receiver. Thus, the thermal energy is lost to the environment quite easily. Therefore, a volumetric solar receiver with $\tau=3$ is less efficient than one with $\tau=1.6$. On the other hand, small optical thickness, for example $\tau=0.5$, causes that all the incoming solar radiation is not absorbed. To obtain the optimum optical thickness for the volumetric receiver, the optimum system efficiency η_{sys}^{opt} was used. Figure 4-5 shows the values achieved with Therminol VP-1 and s-CO₂. In the case of Therminol VP-1, $\tau^{opt}=1.2$, which corresponds to a volume fraction $\phi=8.2\cdot10^{-6}$. In the case of s-CO₂, $\tau^{opt}=1.6$, which corresponds to a volume fraction $\phi=1.5\cdot10^{-5}$. The difference in the results is not only caused by the volume fraction, but also by the different values of the refractive index of these base-fluids. The radiative properties of the carbon nanoparticles were assumed equal for both nanofluids.

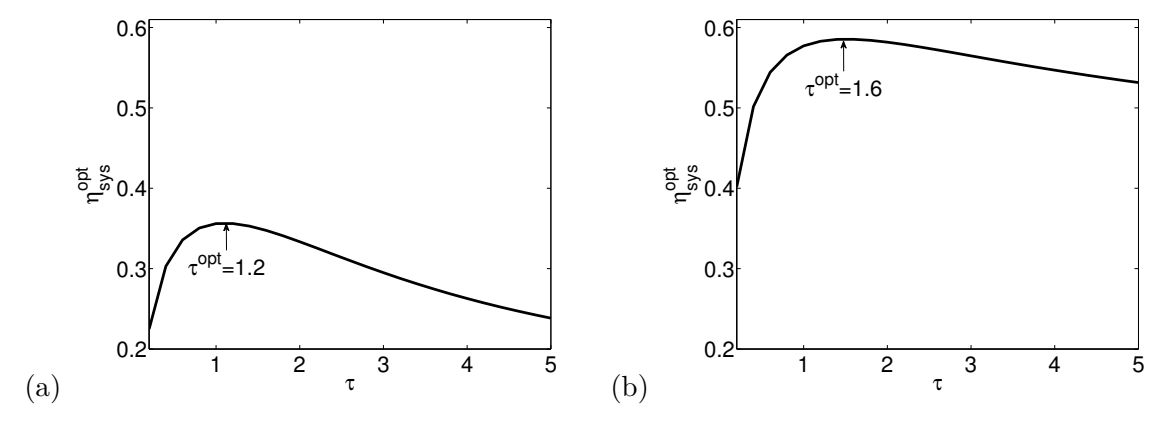


Figure 4-5: Optimum optical thickness τ^{opt} for the study case when C=10, H=2.5cm, T_{in} =400K. (a) Therminol VP-1. (b) s-CO₂.

Effect of Receiver Height

The height of the nanofluid is essential for the design of the volumetric solar receiver. Figure 4-6 shows improvements in the overall system efficiency with increasing the receiver height from 1cm to 20cm. The observed greater efficiency can be attributed to higher volumetric heat generated within the receiver. The sunlight is absorbed by the suspended nanoparticles as it travels through the fluid. Hence, for a solar collector with a greater depth, the amount of incident solar radiation absorbed volumetrically by the nanofluid will be higher, which results in larger fluid temperature, and better efficiencies. Moreover, the spectral intensity of the sunlight is absorbed by the nanoparticles in an exponential form, which is eventually manifested as an asymptotic-type curve. In the volumetric receiver with s-CO₂ with variable properties (Figure 4-6 (b)), the system efficiency increases with receiver height, and reaches an asymptotic value of about 60% for H \geq 5 cm. The same trend is visualized for s-CO₂ with constant properties, but in this case the efficiency reaches an asymptotic value of about 80% for H \geq 5 cm. However, in the case with Therminol VP-1, η_{sys} does not reach its asymptotic value for a receiver height lower than 20 cm. Furthermore, it is observed that increasing the receiver height reduces considerably the length of the receiver.

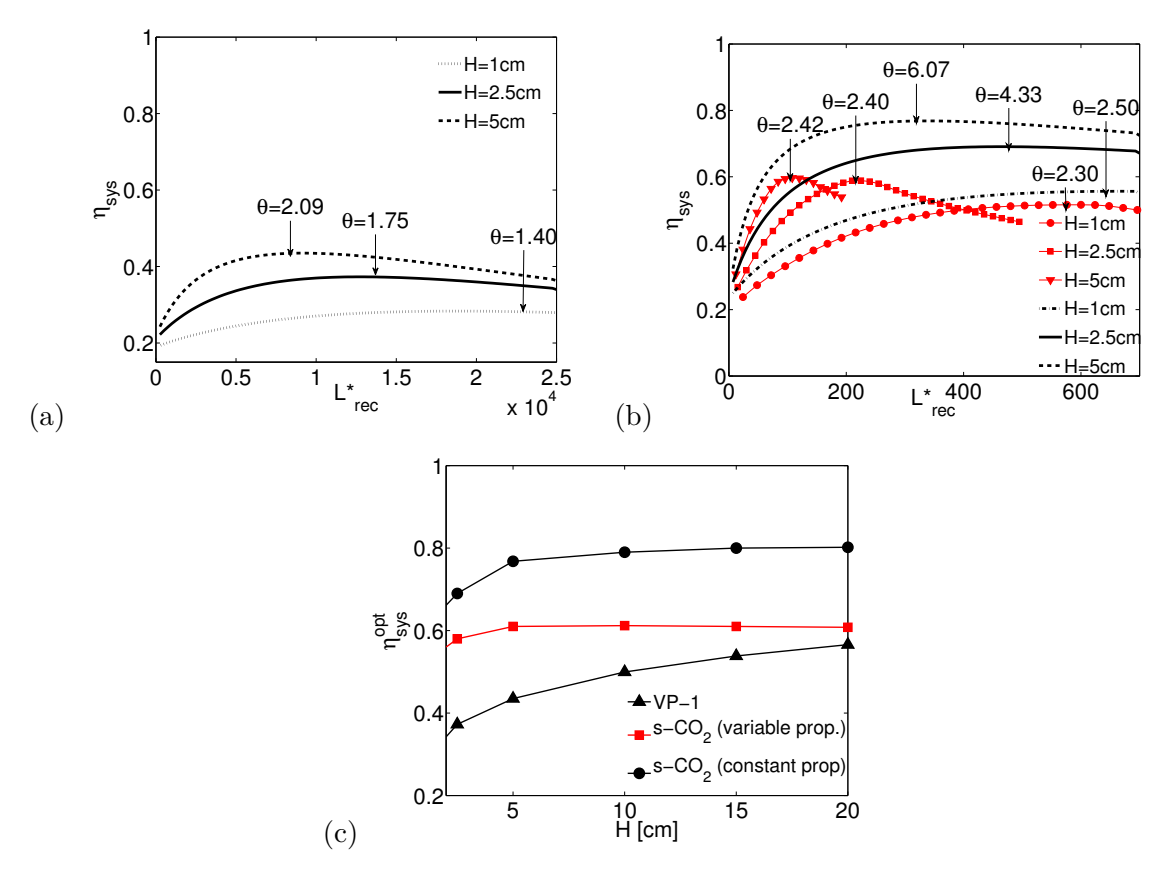


Figure 4-6: Variation of receiver height with constant C=10 and T_{in} =400K. (a) Therminol VP-1 with $\tau_{VP-1}=1.2$. (b) s-CO₂ with $\tau_{s-CO_2}=1.6$. (c) Asymptotic-type curve for both fluids. Constant properties in *black* and variable properties in *red*.

Effect of Solar Concentration Factor

Solar concentration factor represents the amount of incident solar radiation entering the receiver to be absorbed volumetrically by the suspended nanoparticles. The effect of the solar concentration factor on the performance of the overall system was evaluated for a range of C between 5 and 50, which results in heat fluxes from 5 kW/m² to 50 kW/m². Figure 4-7 shows improvements on the system performance and outlet temperature of the receiver with increasing C. The observed trend is attributed to higher volumetric heat generated within the receiver. Moreover, it is observed that increasing C reduces the length of the receiver, which leads to lower footprint and cost of the equipment. As it was explained previously, the spectral intensity of the sunlight is absorbed by the nanoparticles in a exponential form, which is eventually manifested as an asymptotic-type curve. In the case with s-CO₂ with variable properties (Figure 4-7 (b)), the system efficiency increases until it reaches an asymptotic value of about 60% for C ≥ 10 . The same trend is illustrated with s-CO₂ with constant properties. However, the efficiency reaches an asymptotic value of about 80% for C ≥ 30 . Nonetheless, in the case with Therminol VP-1, η_{sys} does not reach its asymptotic value for solar concentration factors lower than 50.

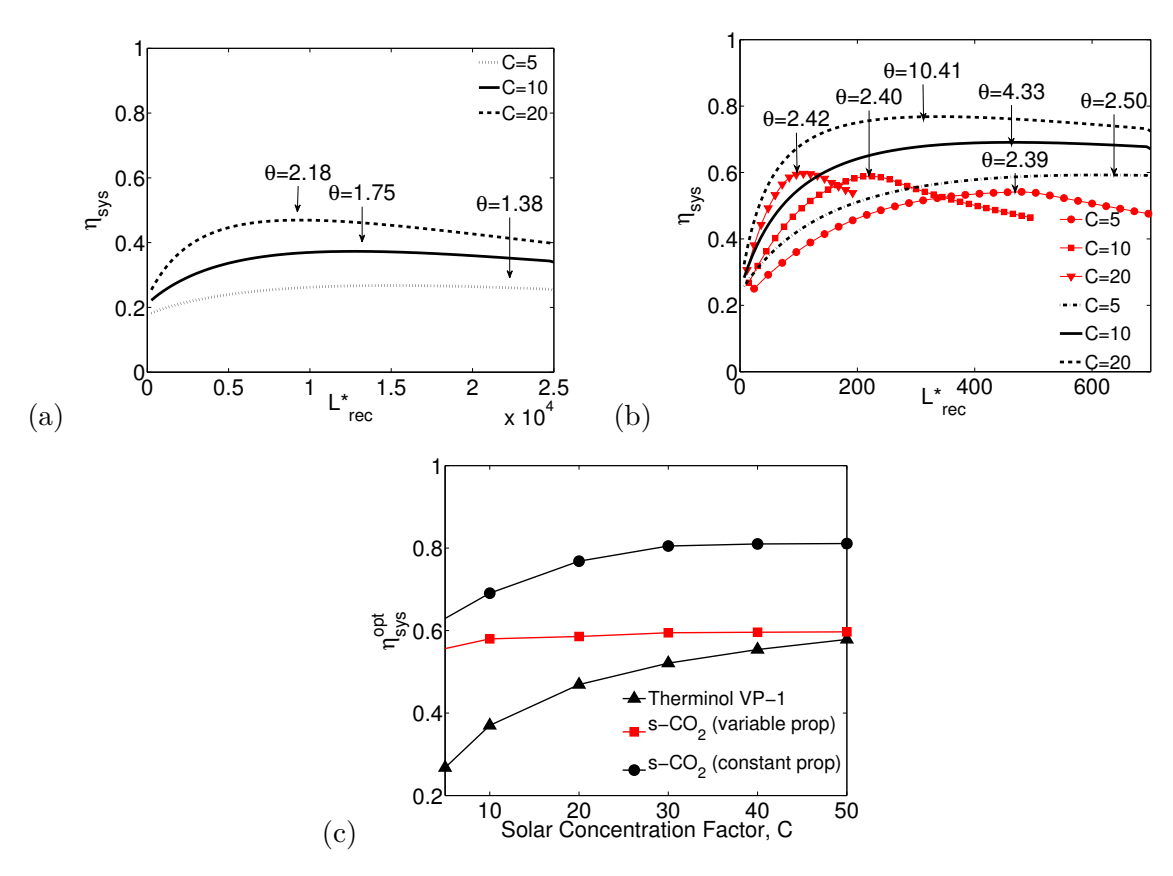


Figure 4-7: Variation of solar concentration factor with constant H=2.5cm and T_{in} =400K. (a) Therminol VP-1 with $\tau_{VP-1}=1.2$. (b) s-CO₂ with $\tau_{s-CO_2}=1.6$. (c) Asymptotic-type curve for both fluids. Constant properties in *black* and variable properties in *red*.

4-2-2 Comparison to surface-based solar receiver

Surface-based solar receivers are designed to absorb as much sunlight as possible while limiting the radiative heat loss from the absorbing surface. The surface of this type of receiver is typically black or spectrally selective such that high absorptivity in the solar spectrum is coupled with low emissivity in the infrared region. In the following analysis, an ideal selective surface receiver with sharp cut-off wavelength at $2\mu m$ is considered. Figure 4-8 shows the spectral dependence on the emissivity. Surface-based receivers are compared with volumetric solar receivers for both base-fluids, Therminol VP-1 and s-CO₂, based on the optimum system efficiency.

In order to quantitatively assess the performance of surface and volumetric systems Figure 4-9 shows the results of both types of receivers for different values of solar concentration factor C. In this analysis, the height and inlet temperature of the solar collectors are kept constant to 2.5cm and 400K, respectively. It is observed that the optimum system efficiency decreases with increasing solar concentration factor in a surface-based receiver. These solar collectors are efficient at solar-to-thermal conversion. However, they are not well suited for transferring heat to a carrier fluid. A large temperature difference between the absorber and the fluid arises at high levels of solar concentration. The temperature difference leads to significant emissive losses at the surface, which results in a low overall system efficiency. On the other hand, the optimum system efficiency improves with increasing solar concentration factor in a volumetric receiver. The observed high efficiency is attributed to the direct absorption of the concentrated solar radiation by the nanoparticles, which results in a more uniform temperature distribution within this type of solar collector. Hence, with a volumetric receiver the temperature difference between the absorber and the fluid decreases, which reduces the emissive losses at higher temperatures, and increases the efficiency.

Figure 4-9 (a) illustrates the comparative analysis between both types of solar collectors with Therminol VP-1 as the base-fluid. It is observed a better performance of the system when a surface-based receiver is coupled to an ideal cycle for low solar concentration factors. However, the trend reverses when C reaches approximately 7 ($\eta_{sys}^{opt} \approx 35\%$), and the overall system begins to achieve higher efficiencies with volumetric receivers. On the other hand, Figure 4-9 (b) shows the comparative analysis between both types of solar collectors with s-CO₂. In this case,

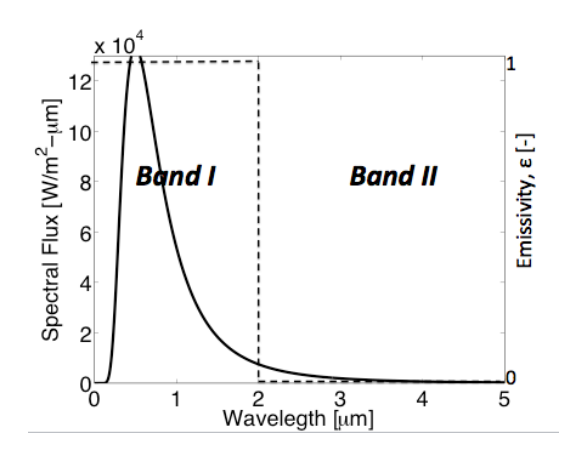


Figure 4-8: Spectral emissivity of an ideal selective surface-based receiver. (—) incident solar flux. (- - -) emissive losses.

the volumetric receiver converts the concentrated solar radiation into thermal energy more efficiently for all values of C. This result is caused because both convection and emissive losses are taken into consideration in the surface-based solar collector, while only convective loss to the surroundings is considered in the volumetric receiver model with s-CO₂ as base-fluid.

Figure 4-10 illustrates the results of both types of solar collectors for different configurations of height, while the solar concentration factor and inlet temperature are kept constant to 10 and 400K, respectively. The same trend as Figure 4-9 is observed. In the study case of Therminol VP-1, a better performance of the system is achieved with surface-based receivers only for $H \leq 2.5$ cm. In the study case with s-CO₂, the performance of the system shows outstanding results when an ideal power generation cycle is coupled to a volumetric receiver. However, Figure 4-10 (b) sketches significantly low values of η_{sys}^{opt} with surface-based solar collectors. Therefore, it can be concluded that the incorporation of a surface-based receiver to the s-CO₂ Brayton cycle can be significantly harmful.

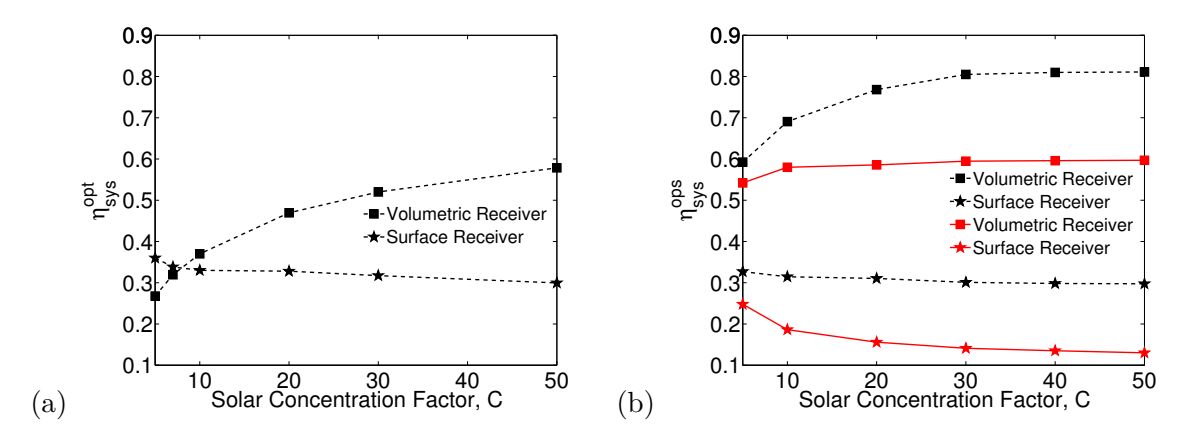


Figure 4-9: Surface Receiver vs. Volumetric Receiver for different solar concentration factors with constant H=2.5cm, $T_{in}=400$ K. (a) Therminol VP-1 (b) s-CO₂. Constant properties in *black* and variable properties in *red*.

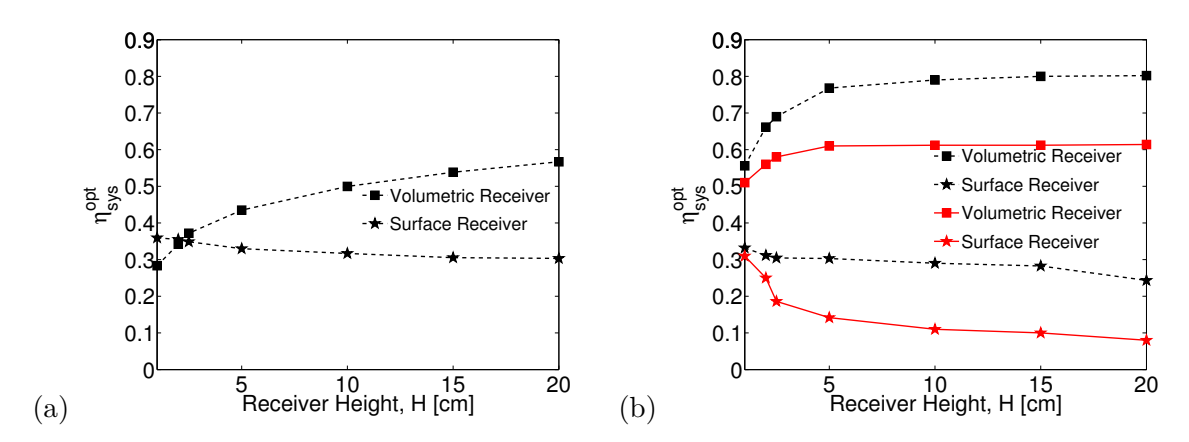


Figure 4-10: Surface Receiver vs. Volumetric Receiver for different receiver height with constant C=10, T_{in} =400K. (a) Therminol VP-1. (b) s-CO₂. Constant properties in *black* and variable properties in *red*.

Master of Science Thesis

4-3 Volumetric Solar Receiver for the s-CO₂ Brayton Cycle

Supercritical carbon dioxide is a promising alternative to optimize the design and performance of volumetric solar receivers at low and mid-temperatures, as it was shown in the previous section. However, the purpose of this thesis is to combine this new solar receiver technology with the s-CO₂ Brayton cycle. In this cycle, the temperature of the exhaust gas leaving the turbine is often considerably higher than the temperature of the s-CO₂ leaving the compressor. Therefore, the high-pressure s-CO₂ leaving the compressor is usually heated up by the hot exhaust gas of the turbine in a counter-flow heat exchanger, which is also known as a regenerator. For that reason, in the s-CO₂ Brayton cycle with regeneration, for solar applications, the solar receiver works at temperatures approximately between 675K ($\approx 400^{o}C$) and 1000K ($\approx 725^{o}C$). In this section, the performance of an ideal s-CO₂ Brayton cycle coupled with a volumetric solar receiver with inlet temperature of 675 K is presented. The results are illustrated in a comparative analysis between low and high inlet temperature of the volumetric solar collector. Furthermore, the influence of varying the thermo-physical properties on the numerical model at high inlet temperature is evaluated.

Gs, Re and Nu are the same values than in the previous section. Moreover, the assumptions stated before remain the same for this section. However, the properties are set to different values:

Constant Properties:

Supercritical CO₂:

- k_{c0} =0.068 W/m K;
- $\rho_0 = 145.42 \text{ kg/m}^3$;
- $Cp_0=1265.10 \text{ J/kg K};$
- $\mu_0 = 3.988 \times 10^{-5} \text{ Pa·s};$
- Pe=1115.10.

Variable Properties:

Supercritical CO₂:

- k_{c0} =0.055 W/m K;
- $\rho_0 = 193.19 \text{ kg/m}^3$;
- $Cp_0=1247.21 \text{ J/kg K};$
- $\mu_0 = 3.425 \times 10^{-5} \text{ Pa·s};$
- $h_0 = 4.605 \times 10^5 \text{ J/kg}$;
- Pe=1165.21.

In order to explore the influence of the inlet temperature of the volumetric solar receiver on the performance of the system, Figure 4-11 shows the optimum system efficiency for low (400 K) and high (675 K) inlet temperatures. The analysis has been carried out for several configurations of C and H.

Figure 4-11 (a) illustrates the effect of varying the solar concentration factor, while the receiver height is kept constant to 2.5cm. η_{sys}^{opt} reaches values up to 67% when the inlet temperature of the volumetric solar receiver is 675 K. The result shows an increment of 7% on the efficiency of the system compared with $T_{in} = 400 K$ of the solar collector. However, it is important to note that at $C \leq 13$, the optimum performance of the system is slightly higher at lower inlet temperature. At low solar concentration, the convection loss, for the case when T_{in} =675 K, is considerably large compared with the solar heat flux entering the volumetric receiver. Therefore, increasing C represents higher solar heat fluxes, which leads to a more significant difference between the heat entering the receiver and the heat loss from the top surface.

Varying H shows the same behavior explained above. Figure 4-11 (b) illustrates the performance of the system for different values of nanofluid height. η_{sys}^{opt} reaches values up to 69% with a volumetric solar receiver with $T_{in} = 675K$, which results in an increment of 9% compared with the case when $T_{in} = 400K$. Nevertheless, at small H, the optimum performance of the system is better with a volumetric solar receiver at $T_{in} = 400K$. As it was explained in the previous section, smaller receiver height represents longer length, which results in larger convective loss to the surroundings. Therefore, increasing H, results in a considerable reduction of the receiver length, which decreases the convection loss to the surroundings.

Finally, it is studied the influence of varying the properties of the volumetric solar receiver model at high inlet temperatures. As noted previously the assumption of constant properties results in overestimation of the system efficiency for low and mid-temperatures. However, at high temperatures of s-CO₂ the properties behave linearly and in some cases, as for example Cp, the variation is negligible ($\leq 5\%$) when the temperature is higher than 650K. Therefore, the effect of properties variation should be studied in this section. Figure 4-11 shows in black the results of constant properties and in red the results of variable properties. The plot shows a considerable increase on the efficiency of the system when the properties are kept constant, which result in an overestimation of the receiver performance. The difference of the η_{sys}^{opt} , for constant and variable properties, is approximately between 10-13% in both cases. Therefore, assuming constant properties in the nanofluid-based volumetric receiver with s-CO₂ as base-fluid will give inaccurate results.

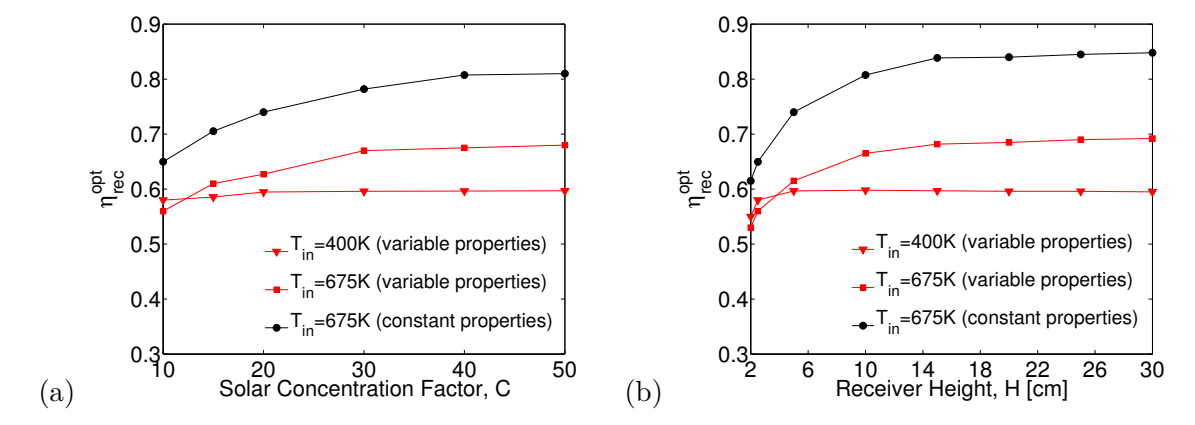


Figure 4-11: s-CO $_2$ optimum system efficiency; effect of inlet temperature and properties variation. (a) Different solar concentration factor with constant H=2.5cm and τ =1.6. (b) Different receiver height with constant C=10 and τ =1.6. Constant properties in *black* and variable properties in *red*.

D. C. Hernandez Aita

Conclusions and Recommendations

Conclusions

In the present work, nanofluid-based solar receivers have been investigated. A 2-D steady-state numerical model has been developed to predict the temperature profile and performance of volumetric receivers based on the direct absorption by nanoparticles. In addition, the model is used to propose design guidelines of the solar collector based on the optimum system efficiency.

Supercritical carbon dioxide has been studied as a feasible base-fluid for solar receivers. The advantages of implementing s-CO₂ in volumetric absorption systems were assessed by comparison with a conventional base-fluid commonly used for mid-temperature solar applications called Therminol VP-1. The analysis was carried out for a 2.5cm receiver height with 10 suns of incident radiation (CGs=10 kW/m²), and an inlet temperature of 400K. Optimizations in the design and performance of the nanofluid-base solar receiver were found when the base-fluid was substituted from Therminol VP-1 to s-CO₂. The overall system performance was improved by 20%, and the outlet temperature of the solar collector increased approximately $250^{\circ}C$. Additionally, it was shown that the length of the receiver reduced considerably, which decreases the cost and footprint of the equipment.

The influence of variation thermo-physical properties was investigated for solar collectors with $s-CO_2$ as base-fluid. It was observed that constant properties overestimated the performance and temperature within the receivers. Therefore, assuming constant properties gives unrealistic results.

The numerical model was used to explore the influence of varying the optical thickness τ , the receiver height H, and the solar concentration factor C on the efficiency of the system. It was demonstrated that there is an optimum optical thickness at which volumetric collectors with nanofluid perform the best. The performance of the overall system was found to be the highest for an optical thickness of 1.6 in the study case with s-CO₂, and 1.2 in the study case with Therminol VP-1. In general, the system performance enhances with increasing nanofluid height and solar concentration factor. The overall system reaches efficiencies up to

60% when is coupled with a volumetric solar receiver, with s-CO₂ (variable properties) and carbon nanoparticles as working fluid, for C \geq 10 and H \geq 5cm.

Nanofluid-base solar receivers were compared to surface-based solar receivers based on the optimum performance of the system. In general, the numerical results revealed that the volumetric collectors have the potential to harness solar radiant energy more efficiently as compared to conventional collectors for different configurations of receiver height and incident solar concentration. However, in the study case with Therminol VP-1, surface receivers showed better system efficiencies when $C \le 7$ and $H \le 2.5$ cm.

In the final part of this work, the volumetric solar receiver with s-CO₂, as base-fluid, was evaluated at a high inlet temperature of 675 K. The purpose of this investigation was to study if this new solar collector technology may be integrated in the s-CO₂ Brayton cycle for CSP plants. The results were illustrated in a comparative analysis between low (400K) and high (675K) inlet temperature of the receiver. It was observed that increasing the inlet temperature of the solar collector enhances the efficiency of the system. Furthermore, it was shown that the performance of an ideal s-CO₂ Brayton cycle combined with a nanofluid-based solar receiver has the potential to reach efficiencies up to 68% when C>30 and H>15cm.

The results above are encouraging, and aim to provide helpful starting point for the development of volumetric solar receivers for the s- $\rm CO_2$ Brayton cycle in solar applications. However, given the uncertainties in terms of stability, oxidation and distribution, among others, of the carbon nanoparticles in s- $\rm CO_2$ more research have to be done in this subject.

Recommendations for future work

To reduce the complexity of the coupled energy and radiative equations, the numerical model developed in this thesis has been based on several simplifications. In order to obtain a more realistic volumetric solar receiver, the momentum equation should be included in the governing equations. Furthermore, future work should involve the study of nanoparticle distribution within the nanofluid. Additionally, due to most flows in the industry are turbulent, fundamental studies of nanoparticles in turbulent flow should be investigated.

In terms of experimental research, the current mathematical analysis needs to be substantiated with experiments in order to transform this novel concept into a commercial reality. An experimental set up to study the oxidation of carbon nanoparticles and their stability in supercritical carbon dioxide should be developed. Moreover, the radiative properties of CO_2 at high pressures should be investigated. The absorption characteristics of CO_2 have been reported for pressures not higher than 40 bar, which is considerably lower than the pressure of the volumetric solar receiver for the s- CO_2 Brayton cycle.

Appendix A

MATLAB Code

A-1 Volumetric solar receiver with variable properties

```
3
                         FLUIDPROP
  5
  load('CO2250bar.mat');
6
  \texttt{temp} \hspace{-0.05cm}=\hspace{-0.05cm} \texttt{CO2250bar} \hspace{0.05cm} (\hspace{0.05cm}:\hspace{0.05cm}, 1\hspace{0.05cm}) \hspace{0.1cm};
                                            % [C]
9 temperature=C02250bar(:,1) +273.15;
                                            %[K]
10 rho_dim=C02250bar(:,2);
                                            %[kg/m3]
11 mu_dim=C02250bar(:,3);
                                            %[Pa.s]
12 kc_dim=C02250bar(:,4);
                                            %[W/mK]
13 heatcapacity_dim=C02250bar(:,5);
                                            %[kJ/kgK]
  enthalpy_dim=C02250bar(:,6);
                                            %[KJ/kg]
  Cp_dim = 1000.*heatcapacity_dim;
                                            %[J/kgK]
16 h_dim = 1000.*enthalpy_dim;
                                            %[J/kg]
17
INITIAL CONDITIONS
21 tau = 1.6;
                                            %optical thickness
22 H = 0.025;
                                            %height [m]
23 Tamb = 300;
                                            %ambient temperature [K]
24 \text{ Tin} = 400;
                                            %inlet temperature of
     nanofluids [K]
25 C=20;
                                            %solar concentration factor [-]
                                            %Incident solar radiation [W/m2
26 Gs = 1000;
27 epsilon=0;
                                            %emissivity
28 \quad \mathtt{sigma} \!=\! 5.67 \mathtt{e} \!-\! 8;
                                            %Stefan-Boltzmann constant;
```

46 MATLAB Code

```
29
30
33 %
                    PROPERTIES
                                              %
35 rho 0=interp1(temperature, rho dim, Tin);
                                     %density [Kg/m<sup>3</sup>]
36 mu_0=interp1(temperature, mu_dim, Tin);
                                     %dynamic viscosity [Pa.s]
37 v_0=mu_0/rho_0;
                                     %kinematic viscosity [m2/s]
38 kc_0=interp1(temperature,kc_dim,Tin);
                                     %thermal conductivity [W/mK]
39 Cp_0=interp1(temperature,Cp_dim,Tin);
                                     %heat capacity [J/KgK]
40 h_0=interp1(temperature,h_dim,Tin);
                                     %enthalpy [J/kg]
41
42 %optical
43 np = 2.72;
                                     %refractive index of particle
44 kp = 1.31;
                                     %absorption index of particle
                                     %refractive index of fluid
45 nf = 1.11;
46 m=complex(np/nf,kp/nf);
47 K1 = imag((m^2-1)/(m^2+2));
48
50 h=6.626e-34;
                                     %Planck's constant [J.s]
51 c = 299792458;
                                     %speed of light [m/s]
52 Kb=1.3807e-23;
                                     %Boltzamann's constant [J/K]
54
DIMENSIONLESS VALUES
56 %
58 Re = 1500;
                                     %laminar flow
                                     %Prandlt Number
59 Pr=Cp_0*mu_0/kc_0;
60 Pe=Pr*Re;
                                     %Peclet Number
61
                                     %Nusselt Number (heH/Kc)
62 Nu=1;
63
64 R=(C*Gs*H)/(Tin*kc_0);
                                     %dimensionless number
65 St=epsilon*sigma*H*(Tin^3)/kc_0;
                                     %Stefan Number
  teta_amb=Tamb/Tin;
                                     %dimensionless ambient
66
     temperature
  theta=temperature/Tin;
69 %Properties
70 rho_1=rho_dim/rho_0;
71 mu_1=mu_dim/mu_0;
72 kc_1=kc_dim/kc_0;
73 Cp_1=Cp_dim/Cp_0;
74 h_1=h_dim/h_0;
75
77 %
                                              %
                  DISCRETIZATION
79 He=1:
                                    %dimensionless height
80 L=200;
                                    %dimensionless lenght
```

```
81 Nx = 100;
                                     %number of discretizations
82 Ny=200;
                                     %number of discretizations
83 dx=L/Nx;
                                     %step in x
84 dy=He/Ny;
                                     %step in y
  teta=ones(Ny+1,Nx+1);
                                     %starting point
   teta_Ref = 2*ones(Ny+1,Nx+1);
   n=0;
87
   tol = 100;
88
89
   91
                   VOLUME FRACTION
92
   93
94
   lambda avg=5e-7;
95
   fv = (2*tau*lambda_avg)/(H*6*pi*K1);
96
97
   98
                SOLAR HEAT FLUX GAIN
99
   100
101
102
   for j=1:Ny+1
103
104
      Qgen(j)=Q_gen(fv,H,(dy*(j-1)));
105
106
   end
107
108
109
   110
                TEMPERATURE PROFILE
                                               %
111
   113
   while tol>=0.0001 \& n<200000
114
115
   for j=1:Ny+1
116
      for i=1:Nx+1
117
         kc(j,i)=interp1(theta,kc_1,teta(j,i),'linear','extrap');
118
119
         rho(j,i)=interp1(theta,rho_1,teta(j,i),'linear','extrap');
          if teta(j,i)\leq 1000/\text{Tin};
120
             Cp(j,i)=interp1(theta,Cp_1,teta(j,i),'linear');
121
             h_{enthalpy}(j,i)=interp1(theta,h_1,teta(j,i),'linear');
122
123
          else
             Cp(j,i)=interp1(theta,Cp_1,1000/Tin,'linear');
124
             h_1000=interp1(theta,h_1,1000/Tin,'linear');
125
             h_{enthalpy}(j,i) = Cp(j,i) * (teta(j,i) - (1000/Tin)) + h_{1000};
126
          end
127
128
129
      end
130
   end
131
   for i=1:Nx+1
132
      Uinv=0;
133
```

48 MATLAB Code

```
for j=1:Ny+1
134
                                                 Uinv=rho(j,i)*dy+Uinv;
135
                                end
136
                                U(i)=1/Uinv;
137
                end
138
139
140
               \quad \mathbf{for} \quad \mathbf{j} \! = \! 1 \! : \! \mathtt{N} \mathbf{y} \! + \! 1
141
                        teta(j,1) = 1;
142
                        teta(j,Nx+1)=teta(j,Nx);
143
144
145
146
147
                for i=2:Nx
148
                                E lambda = 0:
                                Nlambda = 300;
149
                                {\tt lambda\_min} = 2000.0 \, {\tt e} - 9;
150
                                lambda max = 30000.0e-9;
151
                                for ii=1:Nlambda
152
                                                 lambda = lambda_min + ii*(lambda_max-lambda_min)/(Nlambda-1);
153
                                                 E_{\text{lambda}} = E_{\text{lambda}} + ((pi*2*h*c^2)/(lambda^5))*(1/(exp((h*c)/(lambda)))*(1/(exp((h*c)/(lambda)))*(1/(exp((h*c)/(lambda)))*(1/(exp((h*c)/(lambda)))*(1/(exp((h*c)/(lambda)))*(1/(exp((h*c)/(lambda))))*(1/(exp((h*c)/(lambda)))*(1/(exp((h*c)/(lambda))))*(1/(exp((h*c)/(lambda))))*(1/(exp((h*c)/(lambda))))*(1/(exp((h*c)/(lambda))))*(1/(exp((h*c)/(lambda))))*(1/(exp((h*c)/(lambda))))*(1/(exp((h*c)/(lambda))))*(1/(exp((h*c)/(lambda))))*(1/(exp((h*c)/(lambda))))*(1/(exp((h*c)/(lambda))))*(1/(exp((h*c)/(lambda))))*(1/(exp((h*c)/(lambda))))*(1/(exp((h*c)/(lambda))))*(1/(exp((h*c)/(lambda))))*(1/(exp((h*c)/(lambda))))*(1/(exp((h*c)/(lambda))))*(1/(exp((h*c)/(lambda))))*(1/(exp((h*c)/(lambda))))*(1/(exp((h*c)/(lambda))))*(1/(exp((h*c)/(lambda))))*(1/(exp((h*c)/(lambda))))*(1/(exp((h*c)/(lambda))))*(1/(exp((h*c)/(lambda))))*(1/(exp((h*c)/(lambda))))*(1/(exp((h*c)/(lambda))))*(1/(exp((h*c)/(lambda))))*(1/(exp((h*c)/(lambda))))*(1/(exp((h*c)/(lambda))))*(1/(exp((h*c)/(lambda))))*(1/(exp((h*c)/(lambda))))*(1/(exp((h*c)/(lambda))))*(1/(exp((h*c)/(lambda))))*(1/(exp((h*c)/(lambda))))*(1/(exp((h*c)/(lambda))))*(1/(exp((h*c)/(lambda))))*(1/(exp((h*c)/(lambda))))*(1/(exp((h*c)/(lambda))))*(1/(exp((h*c)/(lambda))))*(1/(exp((h*c)/(lambda))))*(1/(exp((h*c)/(lambda))))*(1/(exp((h*c)/(lambda))))*(1/(exp((h*c)/(lambda))))*(1/(exp((h*c)/(lambda))))*(1/(exp((h*c)/(lambda))))*(1/(exp((h*c)/(lambda))))*(1/(exp((h*c)/(lambda))))*(1/(exp((h*c)/(lambda))))*(1/(exp((h*c)/(lambda))))*(1/(exp((h*c)/(lambda))))*(1/(exp((h*c)/(lambda))))*(1/(exp((h*c)/(lambda))))*(1/(exp((h*c)/(lambda))))*(1/(exp((h*c)/(lambda))))*(1/(exp((h*c)/(lambda))))*(1/(exp((h*c)/(lambda))))*(1/(exp((h*c)/(lambda))))*(1/(exp((h*c)/(lambda))))*(1/(exp((h*c)/(lambda))))*(1/(exp((h*c)/(lambda))))*(1/(exp((h*c)/(lambda))))*(1/(exp((h*c)/(lambda))))*(1/(exp((h*c)/(lambda))))*(1/(exp((h*c)/(lambda))))*(1/(exp((h*c)/(lambda))))*(1/(exp((h*c)/(lambda))))*(1/(exp((h*c)/(lambda))))*(1/(exp((h*c)/(lambda))))*(1/(exp((h*c)/(lambda))))*(1/(exp((h*c)/(lambda))))*(1/(exp((h*c)/(l
154
                                                               *Kb*(teta(1,i)*Tin)))-1))*((lambda_max-lambda_min)/Nlambda);
155
                                end
156
                                teta(1,i) = ((teta(2,i)+dy*Nu*teta_amb-St*dy*((E_lambda/(sigma*Tin^4))-dy*Nu*teta_amb-St*dy*((E_lambda/(sigma*Tin^4))-dy*Nu*teta_amb-St*dy*((E_lambda/(sigma*Tin^4))-dy*Nu*teta_amb-St*dy*((E_lambda/(sigma*Tin^4))-dy*Nu*teta_amb-St*dy*((E_lambda/(sigma*Tin^4))-dy*Nu*teta_amb-St*dy*((E_lambda/(sigma*Tin^4))-dy*Nu*teta_amb-St*dy*((E_lambda/(sigma*Tin^4))-dy*Nu*teta_amb-St*dy*((E_lambda/(sigma*Tin^4))-dy*Nu*teta_amb-St*dy*((E_lambda/(sigma*Tin^4))-dy*Nu*teta_amb-St*dy*((E_lambda/(sigma*Tin^4))-dy*Nu*teta_amb-St*dy*((E_lambda/(sigma*Tin^4))-dy*Nu*teta_amb-St*dy*((E_lambda/(sigma*Tin^4))-dy*Nu*teta_amb-St*dy*((E_lambda/(sigma*Tin^4))-dy*Nu*teta_amb-St*dy*((E_lambda/(sigma*Tin^4))-dy*Nu*teta_amb-St*dy*((E_lambda/(sigma*Tin^4))-dy*Nu*teta_amb-St*dy*((E_lambda/(sigma*Tin^4))-dy*Nu*teta_amb-St*dy*((E_lambda/(sigma*Tin^4))-dy*Nu*teta_amb-St*dy*((E_lambda/(sigma*Tin^4))-dy*Nu*teta_amb-St*dy*((E_lambda/(sigma*Tin^4))-dy*Nu*teta_amb-St*dy*((E_lambda/(sigma*Tin^4))-dy*Nu*teta_amb-St*dy*((E_lambda/(sigma*Tin^4))-dy*Nu*teta_amb-St*dy*((E_lambda/(sigma*Tin^4))-dy*Nu*teta_amb-St*dy*((E_lambda/(sigma*Tin^4))-dy*Nu*teta_amb-St*dy*((E_lambda/(sigma*Tin^4))-dy*Nu*teta_amb-St*dy*((E_lambda/(sigma*Tin^4))-dy*Nu*teta_amb-St*dy*((E_lambda/(sigma*Tin^4))-dy*Nu*teta_amb-St*dy*((E_lambda/(sigma*Tin^4))-dy*Nu*teta_amb-St*dy*((E_lambda/(sigma*Tin^4))-dy*Nu*teta_amb-St*dy*((E_lambda/(sigma*Tin^4))-dy*Nu*teta_amb-St*dy*((E_lambda/(sigma*Tin^4))-dy*Nu*teta_amb-St*dy*((E_lambda/(sigma*Tin^4))-dy*Nu*teta_amb-St*dy*((E_lambda/(sigma*Tin^4))-dy*Nu*teta_amb-St*dy*((E_lambda/(sigma*Tin^4))-dy*Nu*teta_amb-St*dy*((E_lambda/(sigma*Tin^4))-dy*Nu*teta_amb-St*dy*((E_lambda/(sigma*Tin^4))-dy*Nu*teta_amb-St*dy*((E_lambda/(sigma*Tin^4))-dy*Nu*teta_amb-St*dy*((E_lambda/(sigma*Tin^4))-dy*Nu*teta_amb-St*dy*((E_lamba/(sigma*Tin^4))-dy*Nu*teta_amb-St*dy*((E_lamba/(sigma*Tin^4))-dy*Nu*teta_amb-St*dy*((E_lamba/(sigma*Tin^4))-dy*Nu*teta_amb-St*dy*((E_lamba/(sigma*Tin^4))-dy*Nu*teta_amb-St*dy*((E_lamba/(sigma*Tin^4))-dy*Nu*teta_amb-St*dy*((E_lamba/(sigma*Tin^4))-dy*Nu
                                               teta amb^4))/(Nu*dy+1));
157
                                dma = zeros(Ny-1,1);
158
159
                                dmb = zeros(Ny-1,1);
160
                                dmc = zeros(Ny-1,1);
                                RHS = zeros(Ny-1,1);
161
                                res = zeros(Ny-1,1);
162
                                for j=2:Ny
163
                                                                                                                           - (kc(j-1,i)+kc(j,i))/(2*dy*dy);
                                             dma(j-1) =
164
                                             dmb(j-1) = (U(i)*((Cp(j,i-1)+Cp(j,i))/2)*((rho(j,i-1)+rho(j,i))
165
                                                            (2)*Pe/dx) + (2*kc(j,i)+kc(j+1,i)+kc(j-1,i))/(2*dy*dy)+(2*kc(j,i))
                                                           i)+kc(j,i+1)+kc(j,i-1))/(2*dx*dx);
                                             dmc(j-1) =
                                                                                                                           - (kc(j+1,i)+kc(j,i))/(2*dy*dy);
166
                                             \mathtt{RHS}\,(\,\mathtt{j}\,-1) \;=\;\; \mathtt{R}\,\ast\,\mathtt{Qgen}\,(\,\mathtt{j}\,) \;\;+\;\; \mathtt{teta}\,(\,\mathtt{j}\,,\mathtt{i}\,-1)\,\ast\,(\,(\,\mathtt{U}\,(\,\mathtt{i}\,)\,\ast\,(\,(\,\mathtt{Cp}\,(\,\mathtt{j}\,,\mathtt{i}\,-1)\,+\,\mathtt{Cp}\,(\,\mathtt{j}\,,\mathtt{i}\,)\,)\,/\,2)
167
                                                            *((rho(j,i-1)+rho(j,i))/2)*Pe/dx)+(((kc(j,i-1)+kc(j,i))/2)/(dx*)
                                                           dx)))+teta(j,i+1)*(((kc(j,i+1)+kc(j,i))/2)/(dx*dx));
168
                                end
                                \mathtt{dmb}\,(\,\mathtt{Ny}\,-1) \,=\, (\,\mathtt{U}\,(\,\mathtt{i}\,)\,*\,(\,(\,\mathtt{rho}\,(\,\mathtt{j}\,,\,\mathtt{i}\,-1)\,+\,\mathtt{rho}\,(\,\mathtt{j}\,,\,\mathtt{i}\,)\,)\,/\,2\,)\,*\,(\,(\,\mathtt{Cp}\,(\,\mathtt{j}\,,\,\mathtt{i}\,-1)\,+\,\mathtt{Cp}\,(\,\mathtt{j}\,,\,\mathtt{i}\,)\,)\,/\,2\,)\,*
169
                                               Pe/dx) + (kc(j-1,i)+kc(j,i))/(2*dy*dy)+(2*kc(j,i)+kc(j,i+1)+kc(j,i)
                                               -1))/(2*dx*dx); % Neumann boundary condition
170
                                RHS(1)
                                                                        = RHS(1) + teta(1,i)*(kc(1,i)+kc(2,i))/(2*dy*dy);
171
                                res = thomas(dma, dmb, dmc, RHS, Ny-1);
172
173
                                for j=1:Ny-1
174
                                             teta(j+1,i) = res(j);
175
                                end
176
                                teta(Ny+1,i)=teta(Ny,i);
177
178
```

```
179
180
    end
181
182
    for i=1:Nx+1
183
184
        for j=1:Ny+1
             h_{mean}(j,i)=rho(j,i)*U(i)*h_{enthalpy}(j,i);
185
             teta_mean(j,i)=interp1(h_1,theta,h_mean(j,i),'linear','extrap');
186
        end
187
188
    end
189
    for j=1:Ny+1
190
        \begin{array}{ll} \textbf{for} & \textbf{i} = 2 : \texttt{Nx} + 1 \end{array}
191
192
             tol_vector=abs(teta(j,i)-teta_Ref(j,i));
193
        end
194
    end
195
    tol=max(tol_vector);
196
197
    for j=1:Ny+1
198
199
        for i=2:Nx+1
200
             teta_Ref(j,i)=teta(j,i);
201
        end
202
   end
203
   n=n+1;
204
   thetaIntOut = 0;
205
206
    for j=1:Ny
207
      thetaIntOut = thetaIntOut + (teta(j+1,Nx)+teta(j,Nx))*0.5*dy/He;
      tempOut=thetaIntOut*Tin;
208
209
    end
210
211
   output(1) = n;
212
213 output(2) = thetaIntOut;
output (3)=tempOut;
215 \operatorname{output}(4) = \operatorname{tol};
   disp(output)
216
217
218
219
    end
220
221
    for j=1:Ny+1
222
        for i=1:Nx+1
223
             T(j,i)=teta(j,i)*Tin;
        end
224
225
226
    227
                            EFFIENCY
228
229
    230
   Y = [0:dy:He];
231
```

Master of Science Thesis

50 MATLAB Code

```
X = [0: dx : L];
232
233
234 h_avg=mean(h_mean);
   teta_avg=mean(teta_mean);
   T_avg=mean(T);
236
237
    for j=1:Ny+1
238
239
        Qsurf(j)=dy*H*((C*Gs*Q_gen(fv,H,(dy*(j-1))))/H);
240
241
    end
242
    Qin=sum(Qsurf);
243
244
245
    for i=1:Nx+1
246
        eff_rec(i) = (kc_0*h_0*Pe*(h_avg(i)-1))/(Qin*X(i)*H*Cp_0);
        eff_carnot(i)=1-(teta_amb/teta_avg(i));
247
        eff_tot(i)=eff_carnot(i)*eff_rec(i);
248
249
    end
250
   [eff_tot_optimum, position]=max(eff_tot);
251
   Tout_optimum=T_avg(position) - 273.15;
252
253 teta_out_optimum=teta_avg(position);
```

A-1-1 Volumetric Heat Generated

```
1
   2
                 function Heat_Gen = Q_gen(fv,H,Y)
   3
   4
   5 np = 2.72;
                                                                                                                                                                                     %optical property of particle
   6 kp = 1.31;
                                                                                                                                                                                     %optical property of particle
   7 nf = 1.11;
                                                                                                                                                                                     %optical property of fluid
   8 m=complex(np/nf,kp/nf);
   9 K1 = imag((m^2-1)/(m^2+2));
                                                                                                                                                                                     %incident heat flux
10 Gs = 1000;
              C=1:
                                                                                                                                                                                     %solar concentration factor
11
12 Satt = 0.73;
                                                                                                                                                                                    %attenuation constant
13 {\tt omega} = 6.80 {\tt e} - 5;
                                                                                                                                                                                    %solid angle of the sun
14 h=6.626e-34;
                                                                                                                                                                                    %Planck's constant [J.s]
15 c = 299792458;
                                                                                                                                                                                    %speed of light [m/s]
16 Kb=1.3807e-23;
                                                                                                                                                                                    %Boltzamann's constant [J/K]
17
             Tsun = 5800;
                                                                                                                                                                                    %Temperature of sun [K]
18 kv = (6*pi*K1*fv/5e-7);
19
                lambda=1e-9:7e-9:2000e-9;
20
21
              for i=1:286
22
23
24
                 Q1(i) = ((Satt*C*omega*(2*h*(c^2)/(lambda(i)^5))*(1/(exp((h*c/(lambda(i)*Kb)))*(1/(exp((h*c/(lambda(i)*Kb)))*(1/(exp((h*c/(lambda(i))*Kb)))*(1/(exp((h*c/(lambda(i))*Kb)))*(1/(exp((h*c/(lambda(i))*Kb)))*(1/(exp((h*c/(lambda(i))*Kb)))*(1/(exp((h*c/(lambda(i))*Kb)))*(1/(exp((h*c/(lambda(i))*Kb)))*(1/(exp((h*c/(lambda(i))*Kb)))*(1/(exp((h*c/(lambda(i))*Kb)))*(1/(exp((h*c/(lambda(i))*Kb)))*(1/(exp((h*c/(lambda(i))*Kb)))*(1/(exp((h*c/(lambda(i))*Kb)))*(1/(exp((h*c/(lambda(i))*Kb)))*(1/(exp((h*c/(lambda(i))*Kb)))*(1/(exp((h*c/(lambda(i))*Kb)))*(1/(exp((h*c/(lambda(i))*Kb)))*(1/(exp((h*c/(lambda(i))*Kb)))*(1/(exp((h*c/(lambda(i))*Kb)))*(1/(exp((h*c/(lambda(i))*Kb)))*(1/(exp((h*c/(lambda(i))*Kb)))*(1/(exp((h*c/(lambda(i))*Kb)))*(1/(exp((h*c/(lambda(i)))*Kb)))*(1/(exp((h*c/(lambda(i)))*Kb)))*(1/(exp((h*c/(lambda(i)))*Kb)))*(1/(exp((h*c/(lambda(i))))*(1/(exp((h*c/(lambda(i))))*(1/(exp((h*c/(lambda(i)))))*(1/(exp((h*c/(lambda(i)))))*(1/(exp((h*c/(lambda(i)))))*(1/(exp((h*c/(lambda(i)))))*(1/(exp((h*c/(lambda(i)))))*(1/(exp((h*c/(lambda(i))))))*(1/(exp((h*c/(lambda(i)))))*(1/(exp((h*c/(lambda(i)))))*(1/(exp((h*c/(lambda(i)))))*(1/(exp((h*c/(lambda(i)))))*(1/(exp((h*c/(lambda(i)))))*(1/(exp((h*c/(lambda(i)))))*(1/(exp((h*c/(lambda(i)))))*(1/(exp((h*c/(lambda(i))))))*(1/(exp((h*c/(lambda(i))))))*(1/(exp((h*c/(lambda(i)))))*(1/(exp((h*c/(lambda(i)))))*(1/(exp((h*c/(lambda(i)))))*(1/(exp((h*c/(lambda(i)))))*(1/(exp((h*c/(lambda(i)))))*(1/(exp((h*c/(lambda(i))))))*(1/(exp((h*c/(lambda(i)))))*(1/(exp((h*c/(lambda(i)))))*(1/(exp((h*c/(lambda(i)))))*(1/(exp((h*c/(lambda(i)))))*(1/(exp((h*c/(lambda(i)))))*(1/(exp((h*c/(lambda(i)))))*(1/(exp((h*c/(lambda(i)))))*(1/(exp((h*c/(lambda(i)))))*(1/(exp((h*c/(lambda(i)))))*(1/(exp((h*c/(lambda(i)))))*(1/(exp((h*c/(lambda(i)))))*(1/(exp((h*c/(lambda(i)))))*(1/(exp((h*c/(lambda(i)))))*(1/(exp((h*c/(lambda(i)))))*(1/(exp((h*c/(lambda(i)))))*(1/(exp((h*c/(lambda(i)))))*(1/(exp((h*c/(lambda(i)))))*(1/(exp((h*c/(lambda(i)))))*(1/(exp((h*c/(lambda(i)))))*(1/(exp((h*c/(lambda(i)))))*(1/(exp((h*c/
25
                                      *Tsun)))-1))*kv*exp(-kv*(H*Y)))*(2000e-9/286));
                   Q2(i) = ((Satt*C*omega*(2*h*(c^2)/(lambda(i)^5))*(1/(exp((h*c/(lambda(i)*Kb)))*(1/(exp((h*c/(lambda(i)*Kb)))*(1/(exp((h*c/(lambda(i))*Kb)))*(1/(exp((h*c/(lambda(i))*Kb)))*(1/(exp((h*c/(lambda(i))*Kb)))*(1/(exp((h*c/(lambda(i))*Kb)))*(1/(exp((h*c/(lambda(i))*Kb)))*(1/(exp((h*c/(lambda(i))*Kb)))*(1/(exp((h*c/(lambda(i))*Kb)))*(1/(exp((h*c/(lambda(i))*Kb)))*(1/(exp((h*c/(lambda(i))*Kb)))*(1/(exp((h*c/(lambda(i))*Kb)))*(1/(exp((h*c/(lambda(i))*Kb)))*(1/(exp((h*c/(lambda(i))*Kb)))*(1/(exp((h*c/(lambda(i))*Kb)))*(1/(exp((h*c/(lambda(i))*Kb)))*(1/(exp((h*c/(lambda(i))*Kb)))*(1/(exp((h*c/(lambda(i))*Kb)))*(1/(exp((h*c/(lambda(i))*Kb)))*(1/(exp((h*c/(lambda(i))*Kb)))*(1/(exp((h*c/(lambda(i))*Kb)))*(1/(exp((h*c/(lambda(i))*Kb)))*(1/(exp((h*c/(lambda(i))*Kb)))*(1/(exp((h*c/(lambda(i))*Kb)))*(1/(exp((h*c/(lambda(i)))*(exp((h*c/(lambda(i)))*(exp((h*c/(lambda(i))))))*(1/(exp((h*c/(lambda(i)))))*(1/(exp((h*c/(lambda(i)))))*(1/(exp((h*c/(lambda(i)))))*(1/(exp((h*c/(lambda(i)))))*(1/(exp((h*c/(lambda(i)))))*(1/(exp((h*c/(lambda(i)))))*(1/(exp((h*c/(lambda(i)))))*(1/(exp((h*c/(lambda(i)))))*(1/(exp((h*c/(lambda(i)))))*(1/(exp((h*c/(lambda(i))))))*(1/(exp((h*c/(lambda(i)))))*(1/(exp((h*c/(lambda(i)))))*(1/(exp((h*c/(lambda(i)))))*(1/(exp((h*c/(lambda(i)))))*(1/(exp((h*c/(lambda(i)))))*(1/(exp((h*c/(lambda(i)))))*(1/(exp((h*c/(lambda(i)))))*(1/(exp((h*c/(lambda(i)))))*(1/(exp((h*c/(lambda(i)))))*(1/(exp((h*c/(lambda(i)))))*(1/(exp((h*c/(lambda(i)))))*(1/(exp((h*c/(lambda(i)))))*(1/(exp((h*c/(lambda(i)))))*(1/(exp((h*c/(lambda(i)))))*(1/(exp((h*c/(lambda(i)))))*(1/(exp((h*c/(lambda(i)))))*(1/(exp((h*c/(lambda(i)))))*(1/(exp((h*c/(lambda(i)))))*(1/(exp((h*c/(lambda(i)))))*(1/(exp((h*c/(lambda(i)))))*(1/(exp((h*c/(lambda(i)))))*(1/(exp((h*c/(lambda(i)))))*(1/(exp((h*c/(lambda(i)))))*(1/(exp((h*c/(lambda(i)))))*(1/(exp((h*c/(lambda(i)))))*(1/(exp((h*c/(lambda(i)))))*(1/(exp((h*c/(lambda(i)))))*(1/(exp((h*c/(lambda(i)))))*(1/(exp((h*c/(lambda(i)))))*(1/(exp((h*c/(lambda(i)))))*(1/(exp((h*c/(lambda(i)))))*(1/(exp((h*c/(lambda(i)))))
26
                                      *Tsun)))-1))*kv*exp(-kv*(2*H-(H*Y))))*(2000e-9/286));
```

```
27
28 end
29
30 %dimensionless volumetric heat
31
32 VolumetricFluxtop=sum(Q1)*H/(Gs*C);
33 VolumetricFluxbottom=sum(Q2)*H/(Gs*C);
34 Heat_Gen=(VolumetricFluxtop+VolumetricFluxbottom);
35
36 end
```

52 MATLAB Code

Bibliography

- [1] "International energy agency." //http://www.iea.org/, 2014. [Online; accessed 15-May-2014].
- [2] "Statistical review of world energy." //http://www.bp.com/statisticalreview, 2013. [Online; accessed 16-May-2014].
- [3] "Solar technology suitability review." //http://www.energyandresources.vic.gov.au/, 2014. "[Online; accessed 20-May-2014]".
- [4] R. Osuna, R. Olavarria, and R. Morillo, "Ps10, construction of a 11mw solar thermal tower plant in seville, spain," *SolarPACES*, 2006.
- [5] Z. Ma and C. Turchi, "Advanced supercritical carbon dioxide power cycle configurations for use in concentrating solar power systems," *National Renewable Energy Laboratory*, 2001.
- [6] J. B. Noriega, "Design method for s-co₂ gas turbine power plants," Master's thesis, Delft University of Technology, 2012.
- [7] E. Feher, "The supercritical thermodynamic power cycle," Energy Conversion, 1968.
- [8] K. McEnaney, "Modeling of solar thermal selective surfaces and thermoelectric generators," Master's thesis, Massachusetts Institute of Technology, 2010.
- [9] H. Tyagi and P. Phelan, "Predicted efficiency of a low-temperature nanofluid-based firect absorption solar collector," ASME Journal of Solar Energy Engineering, 2009.
- [10] A. Lenert and E. Wang, "Optimization of nanofluid volumetric receivers for solar thermal energy conversion," *Solar Energy*, 2011.
- [11] R. S. Kaluri and S. Dattarajan, "Numerical simulation of direct absorption of solar radiation by a liquid," tech. rep., Siemens Corporate Research & Technologies, 2010.
- [12] A. J. Hunt, "Small particle heat exchangers," Lawrence Berkeley Laboratory, 1978.

54 Bibliography

[13] M. Abdelrahman, P. Fumeaux, and P. Suter, "Study of solid-gas-suspensions used for direct absorption of concentrated solar radiation," *Solar Energy*, 1979.

- [14] S. Kumar and C. L. Tien, "Analysis of combined radiation and convection in a particulate laden liquid film," *Journal of Solar Energy Engineering*, 1990.
- [15] P. Phelan, T. Otanicar, R. Taylor, and H. Tyagi, "Trends and opportunities in directabsorption solar thermal collectors," *Journal of Thermal Science and Engineering Ap*plications, 2013.
- [16] J. A. Hyatt, "Liquid and supercritical carbon dioxide as organic solvents," Journal of Organic Chemistry, 1984.
- [17] E. J. Beckman, "Supercritical and near-critical co2 in green chemical synthesis and processing," *Journal of Supercritical Fluids*, 2004.
- [18] Z. Said, M. Sajid, and R. Saidur, "Radiative properties of nanofluids," *International Communications in Heat and Mass Transfer*, 2013.
- [19] Heat and Mass Transfer in Particulate Suspensions. Springer, 2013.
- [20] E. Michaelides, "Transport properties of nanofluids," Journal of Non-Equilibrium Thermodynamics, 2013.
- [21] A. Einstein, "A new determination of molecular dimensions," Ann. Physics, 1906.
- [22] H. Brickman, "The viscosity of concentrated suspensions in solutions," *Journal Chemistry Physics*, 1952.
- [23] G. Batchelor, "The effect of brownian motion on the bulk stress in a suspension of spherical particles," *Journal of Fluid Mechanics*, 1977.
- [24] S. Maïga, C. Nguyen, N. Galanis, and G. Roy, "Heat transfer behaviours of nanofluids in a uniformly heated tube," *Superlattices and Microstructures*, 2004.
- [25] Y. Xuan and Q. Li, "Heat transfer enhancement of nanofluids," *International Journal of Heat and Fluid Flow*, 2000.
- [26] Y. Xuan and W. Roetzel, "Conceptions for heat transfer correlations of nanofluids," *International Journal of Heat and Mass Transfer*, 2000.
- [27] Y. Xuan and Q. Li, "Stochastic thermal transport of nanoparticle suspensions," *Journal of Applied Physics*, 2006.
- [28] S. Kakac and A. Pramuanjaroenkij, "Review of convective heat and mass transfer enhancement with nanofluids," *International Journal of Heat and Mass Transfer*, 2009.
- [29] S. Z. Heris, M. N. Esfahany, and S. Etemad, "Experimental investigation of convective heat transfer of al₂o₃/water nanofluid in circular pipe," *International Journal of Heat* and Mass Transfer, 2007.
- [30] J. Jung, H. Oh, and H. Kwak, "Forced convective heat transfer of nanofluids in microchannels," *International Journal of Heat and Mass Transfer*, 2009.

- [31] Q. Li and Y. Xuan, "Convective heat transfer and flow characteristics of cu-water nanofluid," *Science in China*, 2002.
- [32] S. T. W. Yang, "Heat transfer augmentation of aqueous suspensions of nanodiamonds in turbulent pipe flow," *Journal of Heat Transfer*, 2009.
- [33] Q. Li and Y. Xuan, "Investigation on convective heat transfer and flow features of nanofluids," *Journal of Heat Transfer*, 2003.
- [34] B. Pak and Y. Cho, "Hydrodynamic and heat transfer study of dispersed fluids with sbumicron metallic oxide particles," Experimental Heat Transfer: A Journal of Thermal Energy Generation, Transport, Storage, and Conversion, 1998.
- [35] A. Sajadi and M. Kazemi, "Investigation of turbulent convective heat transfer and pressure drop of TiO₂/water nanofluid in circular tube," *International Comunications in Heat and Mass Transfer*, 2011.
- [36] R. Pfeffer, S. Rosetti, and S. Licleinm, "Analysis and correlation of heat transfer coefficient and friction factor data for dilute gas-solid suspensions," *International Journal of Heat and Mass Transfer*, 1966.
- [37] W. Dansinger, "Heat transfer to fluidized gas-solid mixtures in vertical transport," Industrial and Engineering Chemistry, 1963.
- [38] L. Farbar and C. Depew, "Heat transfer effects to gas-solids mixtures in a circular tube," *Industrial and Engineering Chemistry*, 1963.
- [39] B. of Meteorology (Australia), "The greenhouse effect and climate change," tech. rep.
- [40] S. Stefani, G. Piccioni, M. Snels, A. Rodin, N. Ignatiev, , and A. Adriani, "Study of the optical properties of co₂ at high pressure and high temperature: comparison between measured and simulated spectra," *Memorie della SocietÃă Astronomica Italiana*, 22.
- [41] S. Stefani, G. Piccioni, M. Snels, A. Rodin, N. Ignatiev, , and A. Adriani, "High pressure/high temperature spectra of co₂; measured and simulated data," *European Planetary Science Congress*, 2010.
- [42] Radiative Heat Transfer. Elsevier Science, 2003.
- [43] A. Michels and J. Hamers, "The effect of pressure on the refractive index of co₂. the lorentz-lorentz formula," *Physica*, 1937.
- [44] C. Adjoury, N. Balu, J. Obriot, and T. Bose, "Simultaneous measurement of dielectric constant and refractive index of sf₆ and co₂ as a function of pressure," *Journal of Chemical Physics*, 1997.
- [45] G. Besserer and D. Robinson, "Refractive indices of ethane, carbon dioxide, and isobutane," *Journal of Chemical Engineering*, 1973.
- [46] J. Cole and N. Halas, "Optimized plasmonic nanoparticle distribution for solar spectrum harvesting," *Applied Letters*, 2006.

56 Bibliography

[47] R. Taylor, P. Phelan, T. Otanicar, and R. Adrian, "Nanofluid optical property characterization: towards efficient direct solar collectors," *Nanoscale Research Letters*, 2011.

- [48] A. Hunt, "Small particle heat exchanger," Lawrence-Berkeley Laboratory, 1978.
- [49] Dimensionless Physical Quantities in Science and Engineering. Elsevier, 2012.
- [50] MATLAB, version 7.10.0 (R2010a). The MathWorks Inc., 2010.
- [51] P. Colonna and T. VanderStelt, FluidProp. 2005.
- [52] A. Veeraragavan, B. Y. A. Lenert, S. Al-Dini, and E. Wang, "Analytical model for the design of volumetric solar flow receivers," *International Journal of Heat and Mass Transfer*, 2012.
- [53] "Therminol vp-1 heat transfer fluid." http://www.therminol.com/products/ Therminol-VP1, 2014. [Online; accessed 19-June-2014].